

**The Cross Section for the Production of $b\bar{b}$ Pairs
in Proton-Antiproton Collisions at $\sqrt{s} = 1.8$ TeV**

A Dissertation

Presented to

The Faculty of the Graduate School of Arts and Sciences
Brandeis University
The Department of Physics

In Partial Fulfillment of the Requirements
for the Degree of

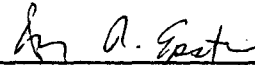
Doctor of Philosophy

by

Robert B. Mattingly
March 1994

This dissertation, directed and approved by the candidate's Committee, has been accepted and approved by the Graduate Faculty of Brandeis University in partial fulfillment of the requirements for the Degree of

DOCTOR OF PHILOSOPHY



Dean, Arts and Sciences

Dissertation Committee:



Craig Blocker, Chairman



Howard J. Schmitzer



Richard Milburn (Tufts University)

Abstract

The Cross Section for the Production of $b\bar{b}$ Pairs in Proton-Antiproton Collisions at $\sqrt{s} = 1.8$ TeV

(A Dissertation presented to the Faculty of the Graduate School of Arts and Sciences of
Brandeis University, Waltham Massachusetts)

by Robert B. Mattingly

The cross section for the inclusive production of $b\bar{b}$ pairs in proton-antiproton collisions at a center-of-mass energy of 1.8 TeV, as measured by the Collider Detector at Fermilab (CDF) during the 1988-1989 experimental run, is presented. The production of bottom quark pairs is identified through the dual semileptonic decay mode, in which one quark produces an electron, and the other a muon. Background from cascade decays of single b quarks is removed by requiring the invariant mass of the $e\mu$ pair be greater than the mass of the b . The $b\bar{b}$ signal is separated statistically from the remaining physics background, $c\bar{c}$ production, by fitting the lepton P_T^{rel} distributions with normalized distributions obtained from Monte Carlo simulations of b and c decays. The resulting cross section, expressed in terms of the b P_T thresholds, is found to be a factor of two higher than the prediction of Quantum Chromodynamics.

Contents

1	Introduction	1
2	Theory	1
2.1	The Structure of the Proton	1
2.1.1	Quarks, Gluons and Color	2
2.1.2	Renormalization and the Strong Coupling Constant	3
2.2	The QCD Improved Parton Model	7
2.2.1	The Parton Distribution Functions	7
2.2.2	Cross Sections	10
2.3	$b\bar{b}$ Production	11
2.3.1	$\mathcal{O}(\alpha_s^2)$	11
2.3.2	$\mathcal{O}(\alpha_s^3)$	11
3	Experimental Apparatus	18
3.1	The CDF Detector	18
3.1.1	Introduction	18
3.1.2	The Vertex Time Projection Chamber	21

3.1.3	The Central Tracking Chamber	22
3.1.4	The Central Calorimetry	27
3.1.5	The Central Muon Chambers	28
3.1.6	The Trigger System	31
4	Electron Identification	33
4.1	Identification of Electron Candidates	33
4.2	Electron Quality Variables	34
4.2.1	LSHR	34
4.2.2	CES χ^2	35
4.2.3	Fiducial Cuts	36
4.2.4	Track Matching	37
4.2.5	HAD/EM	37
5	Muon Identification	39
5.1	Identification of Muon Candidates	39
5.2	Muon Quality Variables	40
5.2.1	Fiducial Cuts	40
5.2.2	Track-Stub Matching	40
5.2.3	Vertex Matching	41
5.2.4	Energy Deposition	41
6	Analysis	42
6.1	The Electron-Muon Data Sets	42
6.1.1	The Analysis $e\mu$ Data Set	42

6.1.2	The Unbiased $e\mu$ Data Set	42
6.2	Method	43
6.2.1	Sources of Electron-Muon Pairs	43
6.2.2	The Method for Measuring $\sigma(b\bar{b}X)$	45
6.2.3	The Survival Fraction $f_{surv}^{(1)}$	49
6.3	Determining $f_{b\bar{b}}$	52
6.3.1	The Relative Transverse Momentum P_T^{rel}	52
6.3.2	Jet Clustering	52
6.3.3	Monte Carlo Distributions	53
6.3.4	Fits to Data	54
6.3.5	Results	56
6.4	Cuts Efficiency ϵ_{cuts}	73
6.5	Acceptances	85
6.5.1	Peterson Fragmentation	85
6.5.2	The ISGW Model	86
6.5.3	The Acceptance	86
6.6	Trigger Efficiency	95
6.6.1	The Trigger Requirements	95
6.6.2	The Total Trigger Efficiency	102
6.7	Results	115
6.7.1	The Inclusive $b\bar{b}$ Cross Section	115
6.7.2	The Single Inclusive b Cross Section	116
6.7.3	The $e\mu$ Transverse Opening Angle	117

7 Conclusion and Future Prospects	121
7.0.4 Conclusion	121
7.0.5 The Future of $b\bar{b}$ Physics at CDF	122

List of Tables

6.1	Electron-muon data set requirements	43
6.2	Summary of $P_T^{rel}(e)$ fit results.	55
6.3	A summary of the uncertainties associated with $f_{b\bar{b}}$	57
6.4	ϵ_1 and component efficiencies.	74
6.5	ϵ_{cuts} as a function of $P_T(\mu)$	75
6.6	$P_T^{min}(b)$ as a function of $P_T(lepton)$	87
6.7	Acceptance of electrons and muons from b decays.	88
6.8	The results of gaussian fits to the E_T^{L2}/E_T^{ELES} distributions for electron volunteers. The rows represent intervals in E_T^{ELES}	100
6.9	The results of gaussian fits to the sign-subtracted E_T^{L2}/E_T^{ELES} distributions for electrons passing the $e\mu$ trigger. The rows represent intervals in E_T^{ELES}	101
6.10	The total trigger efficiency.	102
6.11	Quantities used in the calculation of the cross section for $p\bar{p} \rightarrow b\bar{b} X$	115

List of Figures

2.1	Example of a QCD scattering diagram.	4
2.2	Gluon and quark loops.	5
2.3	An example of parton distribution functions.	9
2.4	The Born level diagrams for $b\bar{b}$ production.	13
2.5	Examples of virtual correction diagrams that contribute to $b\bar{b}$ production.	14
2.6	Examples of diagrams that contribute to $b\bar{b}$ production at $\mathcal{O}(\alpha_s^3)$	15
2.7	Theoretical prediction for $\sigma(b\bar{b} X)$	16
2.8	Theoretical prediction for $\sigma(b\bar{b} X)$ versus $P_T^{min}(\bar{b})$	17
3.1	Isometric view of the CDF detector.	19
3.2	Cross section of the forward detector and a portion of the central detector.	20
3.3	Isometric view of two VTPC modules.	23
3.4	Typical distribution of z vertices from CDF events.	24
3.5	Transverse view of the Central Tracking Chamber.	25
3.6	CEM wedge.	28
3.7	Location of the Central Muon Chambers in a wedge.	29

3.8	Cross section in the $r - \phi$ plane of one CMU chambers showing the 16 drift cells.	30
6.1	An illustration of the definition of P_T^{rel}	58
6.2	Likelihood fits to the direct b electron P_T^{rel} distributions from the MNR-based, single- b generator.	59
6.3	Likelihood fits to the indirect b electron P_T^{rel} distributions from the MNR-based, single- b generator.	60
6.4	Likelihood fits of the direct b electron P_T^{rel} distributions from the Isajet generator.	61
6.5	Likelihood fits of the indirect b electron P_T^{rel} distributions from the Isajet generator.	62
6.6	Sign-subtracted electron E_T distribution.	63
6.7	Sign-subtracted electron P_T distribution.	64
6.8	Distance in R between the electron and the nearest jet, ΔR	65
6.9	Likelihood fits of the charm electron P_T^{rel} distributions.	66
6.10	Comparison of the single- b electron P_T^{rel} parameterizations for direct b , indirect b , and charm.	67
6.11	Comparison of the Isajet electron P_T^{rel} parameterizations for direct b , indirect b , and charm.	68
6.12	Likelihood fits to the data to extract $f_{b\bar{b}}$	69
6.13	b -jet containment versus clustering radius.	70
6.14	$f_{b\bar{b}}$ fit systematic.	71

6.15	Likelihood fit to extract $f_{b\bar{b}}$ from the muon P_T^{rel}	72
6.16	Dimuon invariant mass in the J/ψ mass region.	76
6.17	Track-stub intercept matching for muons from J/ψ decays.	77
6.18	Track-stub intercept matching for muons from J/ψ decays.	78
6.19	z displacement from vertex for muons from J/ψ decays.	79
6.20	Track DCA for muons from J/ψ decays.	80
6.21	Likelihood fit to $P_T^{rel}(e)$ with no selection cuts.	81
6.22	Likelihood fit to $P_T^{rel}(e)$ with all selection cuts.	82
6.23	Distributions of electron quality variables for the unbiased $e\mu$ sample.	83
6.24	Distributions of electron and muon quality variables for the unbiased $e\mu$ sample.	84
6.25	$P_T(b)$ for $P_T(\mu) > 3$ GeV/c	89
6.26	$P_T(b)$ for $P_T(\mu) > 4$ GeV/c	90
6.27	$P_T(b)$ for $P_T(\mu) > 5$ GeV/c	91
6.28	$P_T(b)$ for $P_T(e) > 5$ GeV/c	92
6.29	The Peterson fragmentation function.	93
6.30	P_T^{min1} versus P_T^{min2}	94
6.31	Geometry relating muon P_T to angle of incidence at CMU.	104
6.32	Efficiency of the Level 1 muon trigger.	105
6.33	Efficiency of the Level 2 muon trigger.	106
6.34	Comparisons of Level 2 and offline E_T	107
6.35	Comparison estimated and actual Level 2 electron efficiency for volunteers.	108
6.36	The Level 2 E_T response.	109
6.37	Estimated Level 2 threshold for the data.	110

6.38	The efficiency of the Level 2 <i>HAD/EM</i> requirement as determined from ISAJET plus TRGSIM.	111
6.39	The sign-subtracted sum E_T in a cone of 0.4 around the electron.	112
6.40	The sign-subtracted sum E_T in a cone of 0.7 around the electron.	113
6.41	CTC track reconstruction efficiency.	114
6.42	The cross section for $p\bar{p} \rightarrow b\bar{b} X$	118
6.43	The equivalent single-inclusive b cross section.	119
6.44	The electron-muon transverse opening angle.	120

Chapter 1

Introduction

Studies of b production in $p\bar{p}$ collisions provide quantitative tests of perturbative Quantum Chromodynamics (QCD). For processes involving squared momentum transfers on the order of m_b^2 , the strong coupling constant, α_s , becomes relatively small and perturbative methods are expected to work well. Measurements of the inclusive cross section for $p\bar{p} \rightarrow bX$ have been made at UA1 [1] and at CDF [2]. The QCD prediction [14] is in good agreement with the data at $\sqrt{s} = 630$ GeV but is systematically low when compared to the CDF measurements at $\sqrt{s} = 1.8$ TeV. Consideration of the process $p\bar{p} \rightarrow b\bar{b}X$ provides further opportunities to test QCD; in particular, it provides the opportunity to explore the correlated production of bottom quarks.

The remainder of this thesis is organized as follows: Chapter 2 introduces the parton model of $p\bar{p}$ interactions and discusses the theoretical description of $b\bar{b}$ production, chapter 3 describes the CDF detector, chapters 4 and 5 describe the identification of electrons and muons at CDF, the analysis is presented in chapter 6, and chapter 7 summarizes the results of the analysis and provides a brief look at the prospects for the future.

Chapter 2

Theory

To use $p\bar{p}$ collisions as a tool for the investigation of nature, it is necessary to first understand the nature of the proton. The purpose of this chapter is to provide some understanding, though far from exhaustive, of the internal structure of the proton and the theoretical framework that is used to describe the production of b quarks in $p\bar{p}$ collisions.

2.1 The Structure of the Proton

The structure of the proton, as revealed by lepton scattering, is dependent upon the scale of the four-momentum transfer squared, Q^2 , in the collision. At low values of Q^2 , the scattering is elastic and the proton appears to behave as a point-like object. As the Q^2 is increased, the proton begins to manifest internal structure. The cross section for inelastic scattering grows and resonant behavior appears. As Q^2 is increased further, the dependence of the inelastic cross section upon Q^2 nearly disappears. This region was first probed by the deep inelastic scattering experiments that took place at SLAC in the late 1960s [7].

The independence of the cross section from any mass scale was referred to as 'scaling'. This scaling behavior had been predicted by Bjorken [3] and was later shown by Feynman [4] to be consistent with elastic scattering from free, point-like objects, 'partons', within the proton. The partons were later identified as the quarks that had been introduced by Gell-Mann and Zweig in 1964 [5] as a means of ordering the spectrum of known hadronic states. The picture of nucleon structure that emerged as a result of the deep inelastic scattering experiments was referred to as the 'parton model'. As experiments increased Q^2 still further, scaling violations were eventually observed in the inelastic cross section. Scaling violations were explained as an effect of Quantum Chromodynamics (QCD), the theory of strong interactions between quarks. QCD was incorporated into the parton model to produce the 'QCD improved parton model' that is in wide use today. Before describing this model, it is necessary to first introduce some ideas from QCD.

2.1.1 Quarks, Gluons and Color

QCD describes strong interactions as the exchange of spin-1 gluons between spin- $\frac{1}{2}$ quarks. In analogy to electromagnetic interactions, described by Quantum Electrodynamics (QED), the quarks carry a strong charge called 'color' and the strong force is mediated by the gluons which are roughly analogous to the photon. As opposed to electromagnetism where there is only one charge (plus anti-charge), there are three colors (plus associated anti-colors). QCD further differs from QED in that the photon is electrically neutral, whereas gluons themselves carry color, meaning that gluons not only interact with quarks but with other gluons as well.

2.1.2 Renormalization and the Strong Coupling Constant

Due to the mathematically complex nature of QCD, most calculations rely upon perturbative methods. The lowest order perturbative diagram for the interaction of two unlike quarks, q and q' , is shown in figure 2.1. This diagram schematically shows the scattering of the quarks by the exchange of a gluon. Above leading order, diagrams such as those depicted in figure 2.2 must also be taken into account. These 'one loop' diagrams depict the situation in which the exchanged gluon fluctuates into a virtual quark-antiquark pair or a virtual gluon pair. The inclusion of such diagrams introduces divergences into the calculation of scattering amplitudes as the momentum carried by the virtual particles in the loop approaches infinity. This type of divergence is known as an 'ultraviolet' divergence. Such divergences are handled by absorbing the divergent terms into the definition of the coupling constant. The renormalized coupling, that is, the original 'bare' coupling plus the divergences, is treated as the physical observable that must be measured.

A result of renormalizing the theory is that the coupling constant acquires a Q^2 dependence. This is understandable qualitatively by considering the redefinition of the coupling constant. The new 'physical coupling' that has been defined by the addition of the loop diagrams to the bare coupling can be thought of as a point charge surrounded by virtual pairs. For example, virtual electron-positron pairs are continually created and destroyed in the space surrounding a free electric charge. The virtual pairs behave like dipoles and align themselves with the radial field of the charge. At large distances, that is small Q^2 , a test charge feels a smaller coupling because of the screening effect of the virtual pairs. As the Q^2 increases, the screening effect decreases and the test charge feels an increasing coupling.

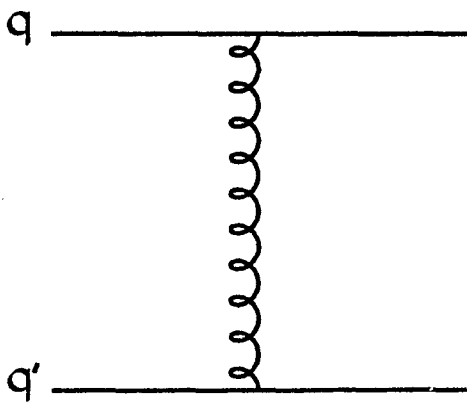


Figure 2.1: The lowest order QCD diagram for the scattering of two unlike quarks.

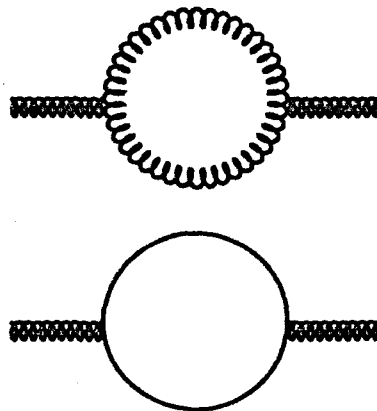


Figure 2.2: An example of gluon and quark one loop diagrams. As the momentum in the loop approaches infinity, the calculated cross section diverges (ultraviolet divergence).

The Q^2 dependence is often referred to as the 'running' of the coupling constant.

Though QCD makes no prediction of the magnitude of the strong coupling, it does provide a relationship showing the evolution of the coupling constant with Q^2 . If the strong coupling constant, α_S , is measured for $Q^2 = \mu^2$, then the value of α_S at some other value of Q^2 is

$$(2.1) \quad \alpha_S(Q^2) = \frac{\alpha_S(\mu^2)}{1 + \alpha_S(\mu^2) \ln(Q^2/\mu^2)}.$$

It is traditional to define α_S in terms of Λ_{QCD}^2 which is the value of Q^2 at which α_S becomes infinite. The expression for Λ_{QCD}^2 is renormalization scheme dependent but a common definition is

$$(2.2) \quad \Lambda_{QCD}^2 = \mu^2 \exp \left[\frac{-12\pi}{(33 - 2N_f)\alpha(\mu^2)} \right],$$

where N_f is the number of quark flavors allowed to participate in the loop diagrams. The expression for α_S is then

$$(2.3) \quad \alpha_S(Q^2) = \frac{12\pi}{(33 - 2N_f) \ln(Q^2/\Lambda_{QCD}^2)}.$$

Once a value for Λ_{QCD}^2 has been provided by experiment, the above equation can be used to obtain a value for α_S at any desired Q^2 . Notice that for $Q^2 \gg \Lambda_{QCD}^2$ the strong coupling becomes small. This is consistent with the observation from the deep inelastic scattering experiments that the scattering centers in the proton behave as quasi-free particles. Note also that it is only in the regime where α_S becomes small that perturbative methods are expected to yield reliable results.

While calculation to all orders in perturbation theory would eliminate the μ^2 depen-

dence, this is usually not possible and some choice of a value for μ^2 must be made. The value chosen for μ^2 usually reflects a momentum scale appropriate for the process in question. Since the μ dependence must disappear in a calculation made to all orders, the sensitivity of a finite order calculation to variations in μ is indicative of the magnitude of the higher order corrections.

2.2 The QCD Improved Parton Model

2.2.1 The Parton Distribution Functions

As in the original parton model, the QCD improved parton model describes the proton in terms of quark constituents. The difference is that now the quarks are allowed to radiate and absorb gluons. The scaling violation that is observed at sufficiently high Q^2 is due to the cloud of gluons surrounding each quark that spreads out the color charge. The scattering center thus gains physical extent which introduces a slight Q^2 dependence into the scattering cross section.

The momentum of a proton is shared amongst its quark and gluon constituents. The parton distribution function, $F_i(x, Q^2)$, represents the probability of a parton of type i having a fraction x of the proton momentum when the proton is probed at a momentum scale of Q^2 . In the original parton model, the proton was composed of three quarks (uud) that combined carry the quantum numbers of the proton. In the QCD improved parton model, these quarks became known as the valence quarks. The term sea quarks represents the quark-antiquark pairs that are constantly being created and destroyed by the color fields of the proton. Figure 2.3 shows some representative parton distribution functions

as a function of x . The figure shows the distributions for valence quarks, gluons, and sea quarks. The valence quark content of the proton is given in terms of the integrated parton distributions functions for up and down quarks

$$(2.4) \quad \int_0^1 dx [F_u(x) - F_{\bar{u}}(x)] = 2$$

$$(2.5) \quad \int_0^1 dx [F_d(x) - F_{\bar{d}}(x)] = 1$$

where $F_{u,d} = F_{u,d}^{valence} + F_{u,d}^{sea}$, $F_{\bar{u},\bar{d}} = F_{\bar{u},\bar{d}}^{sea}$, and the integrations are done at a fixed Q^2 . Parton distribution functions are usually obtained from deep inelastic scattering experiments. The functions thus measured are for a particular value of Q^2 . In order for the functions to be generally applicable, it is necessary to understand how the parton distributions change, or 'evolve', with Q^2 . The QCD predictions for the evolution of the parton distributions with Q^2 are known as the Altarelli-Parisi equations:

$$(2.6) \quad \frac{dF_q(x, Q^2)}{d(\ln Q^2)} = \frac{\alpha_S(Q^2)}{2\pi} \int_x^1 \frac{dw}{w} \left[F_q(w, Q^2) P_{qq}\left(\frac{x}{w}\right) + F_g(w, Q^2) P_{qg}\left(\frac{x}{w}\right) \right],$$

$$(2.7) \quad \frac{dF_g(x, Q^2)}{d(\ln Q^2)} = \frac{\alpha_S(Q^2)}{2\pi} \int_x^1 \frac{dw}{w} \left[\sum_q F_q(w, Q^2) P_{gq}\left(\frac{x}{w}\right) + F_g(w, Q^2) P_{gg}\left(\frac{x}{w}\right) \right].$$

$P_{qq}(z)$ is known as the quark-quark splitting function and describes the probability of a quark emitting a gluon with momentum $1 - z$ and retaining a fraction, z , of its original momentum. P_{qg} , P_{gq} , and P_{gg} are defined analogously. The solutions to the Altarelli-Parisi equations are similar in nature to the expressions for the running coupling constant (Equation 2.1).

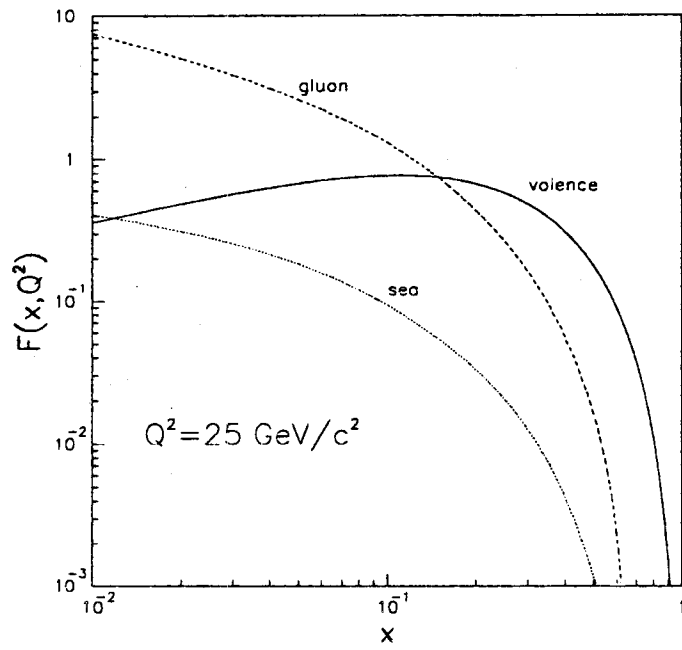


Figure 2.3: An example of the parton distribution functions for the proton. The parameterizations shown are from Diemoz, Ferroni, Longo, and Martinelli (DFLM).

2.2.2 Cross Sections

The calculation of the cross section for the hadroproduction process $AB \rightarrow cX$ is expressed in the improved parton model as the sum of the contributing subprocess cross sections at the parton level, convoluted with the appropriate parton distribution functions.

$$(2.8) \quad \sigma(AB \rightarrow cX) = \int_0^1 dx_a \int_0^1 dx_b F_a(x_a) F_b(x_b) \hat{\sigma}(ab \rightarrow cX).$$

In the above expression, $F_a(x_a)$, represents the probability of finding a parton of type a in hadron A with a fraction, x_a , of the hadrons momentum. The function, $F_b(x_b)$, is defined analogously. The explicit Q^2 dependence of the parton distribution functions has not been shown. The choice made for Q^2 is usually the subprocess center-of-mass (CM) energy, \hat{s} , which is related to the CM energy of the hadronic collision via, $\hat{s} = x_a x_b s$. The subprocess cross section, $\hat{\sigma}$, is the result of calculations at the parton level. To obtain a final state containing observable particles, the hadronization of final state partons must be considered. As hadronization is a low Q^2 process, a description of the process using perturbative QCD is not possible and models must instead be used. The model of fragmentation used in this analysis was the Peterson fragmentation model [18]. Details of this model are given in chapter 6.

As implied in the preceding discussion, the parton model assumes that hadronic interactions can be separated into three, independent phases: the evolution of the partons inside the hadrons prior to the hard scattering, the hard scattering of two partons independent of the remaining hadronic constituents, and the hadronization of the final state partons independent of the initial and intermediate states. This assumption is referred to

as ‘factorization’ and many technical discussions in the context of QCD appear in the literature. A simple, qualitative argument in favor of factorization is known as the ‘impulse’ approximation and will be sketched here. Consider the collision from the point of view of one of the hadrons. The oncoming hadron is highly relativistic and hence, time dilated. For collisions of sufficiently high energy, the dilated lifetime of the virtual hadron states is much larger than the characteristic collision time. This implies that the interacting partons act independently of the remaining hadronic constituents, that is, they act as quasi-free particles.

2.3 $b\bar{b}$ Production

2.3.1 $\mathcal{O}(\alpha_S^2)$

The production of $b\bar{b}$ pairs at $\mathcal{O}(\alpha_S^2)$ in QCD includes only the Born terms. As illustrated in figure 2.4, these terms include only ‘two-to-two’ processes in which a two parton initial state leads to a two parton final state. It is worth noting that at this level in the perturbative calculation, the issue of correlations between the produced bottom quarks is trivial; the quarks are always created back-to-back and with transverse momenta relative to the beam axis (P_T) of equal magnitudes in the center-of-mass frame.

2.3.2 $\mathcal{O}(\alpha_S^3)$

The analysis in this thesis was concerned with the $b\bar{b} X$ final state, meaning that a calculation of the $b\bar{b}$ production cross section to at least $\mathcal{O}(\alpha_S^3)$ was necessary for purposes of comparison. The first full calculation of $b\bar{b}$ production to order $\mathcal{O}(\alpha_S^3)$ was accomplished

by Nason, Mangano, and Ridolfi (MNR) in 1991 [19]. This calculation included the two to three processes shown in figure 2.6 as well as the $\mathcal{O}(\alpha_S^3)$ virtual corrections to the Born terms shown in figure 2.5.

As mentioned previously, perturbative calculations require that some reasonable choice be made for the value of μ ; normally, this choice represents some energy scale relevant to the process under consideration. For the calculation of the $b\bar{b}$ cross section, μ was chosen to be equal to μ_0 , where $\mu_0 \equiv \sqrt{m_b^2 + P_T^2}$ and m_b is the bottom quark mass. Because free quarks have never been observed, m_b is not precisely known. Using potential models of B meson states, m_b is estimated to be in the range 4.5 to 5.0 GeV/ c^2 . Thus, m_b was assumed to be 4.75 GeV/ c^2 . The parton distribution functions used in the calculation were those due to Diemoz, Ferroni, Longo, and Martinelli (DFLM) [6] with $\Lambda_{QCD} = 260$ MeV.

Figure 2.7 shows the result of a $\mathcal{O}(\alpha_S^3)$ calculation for $\sigma(p\bar{p} \rightarrow b\bar{b} X)$. The cross section is shown as a function of the P_T threshold of the b quark, $P_T^{min}(b)$, for $P_T^{min}(\bar{b}) = 8.5$ GeV/ c and absolute rapidities $|y_b| < 1$, $|y_{\bar{b}}| < 1$. The figure clearly demonstrates the non-trivial P_T correlations that have been introduced by the higher-order diagrams. The dashed lines represent the uncertainty involved in the calculation. The uncertainty was obtained by varying the parameters of the calculation in the following ranges: $4.5 < m_b < 5.0$ GeV/ c^2 , $160 < \Lambda_{QCD} < 360$ MeV, $\mu_0/2 < \mu < 2\mu_0$. The cross section was found to be insensitive to variations in m_b and Λ_{QCD} . Thus, the theoretical uncertainty primarily reflects the sensitivity of the cross section to variations in μ . Figure 2.8 shows the variation of the cross section with the P_T thresholds of both the b and \bar{b} . The figure shows the predicted cross section as a function of $P_T^{min}(b)$ for three choices of $P_T^{min}(\bar{b})$. The sensitivity of the cross section to small variations in $P_T^{min}(\bar{b})$ was seen to decrease with increasing $P_T^{min}(b)$.

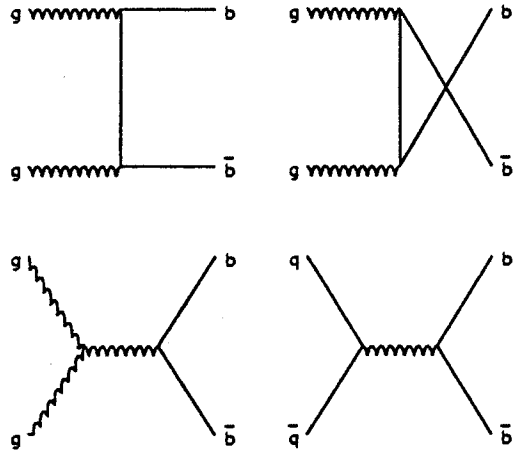


Figure 2.4: The Born level diagrams for $b\bar{b}$ production.

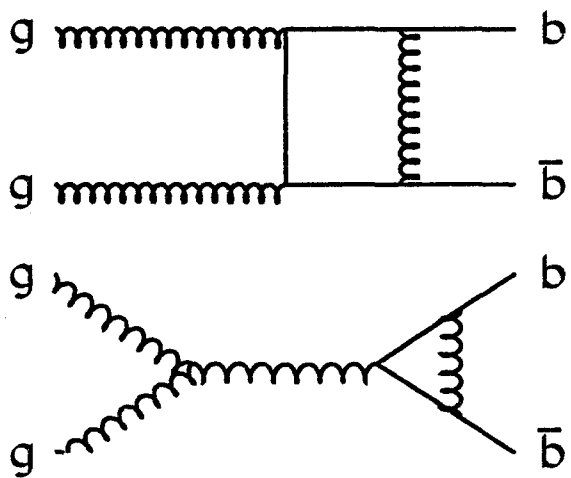


Figure 2.5: Examples of virtual correction diagrams that contribute to $b\bar{b}$ production.

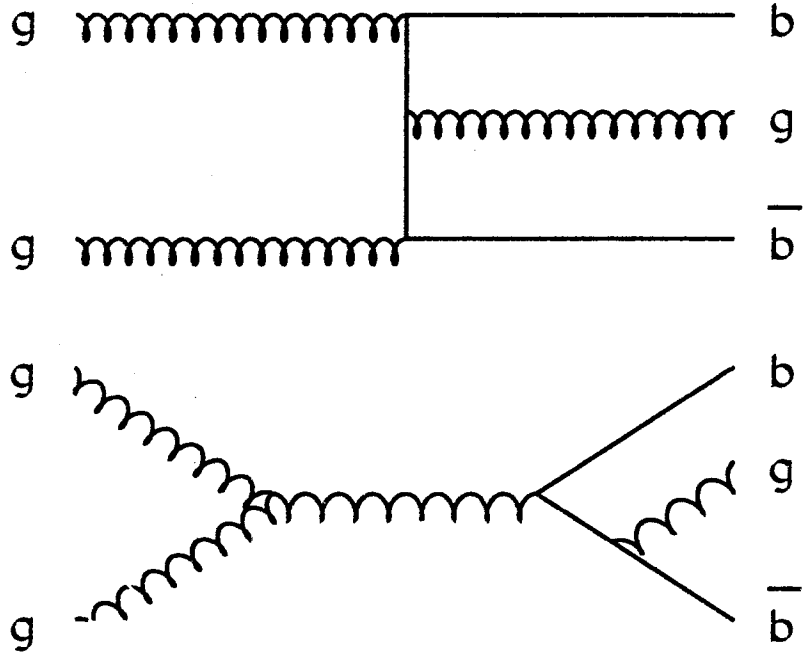


Figure 2.6: Examples of diagrams that contribute to $b\bar{b}$ production at $\mathcal{O}(\alpha_s^3)$.

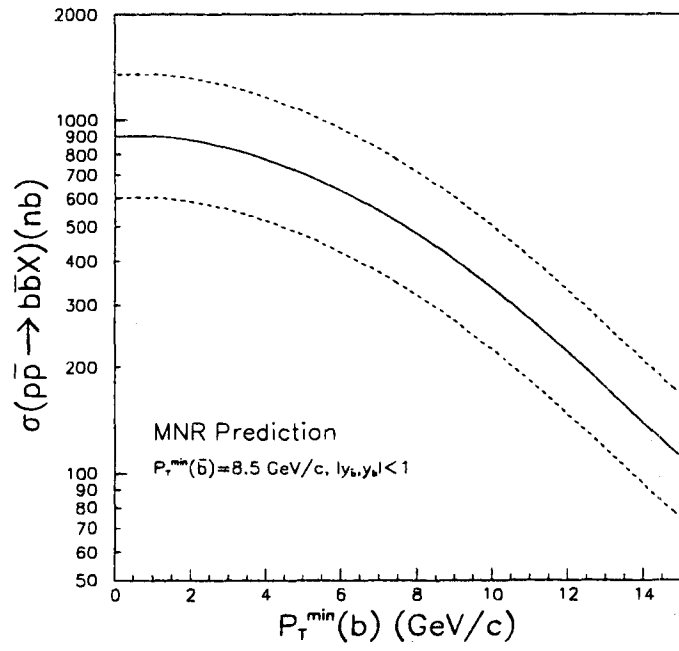


Figure 2.7: Theoretical prediction for $\sigma(p\bar{p} \rightarrow b\bar{b}X)$ from MNR. The cross section is shown as a function of $P_T^{\min}(b)$ for $P_T^{\min}(\bar{b}) = 8.5 \text{ GeV/c}$, and $|y_b, y_{\bar{b}}| < 1$. The dashed lines represent the theoretical uncertainty.

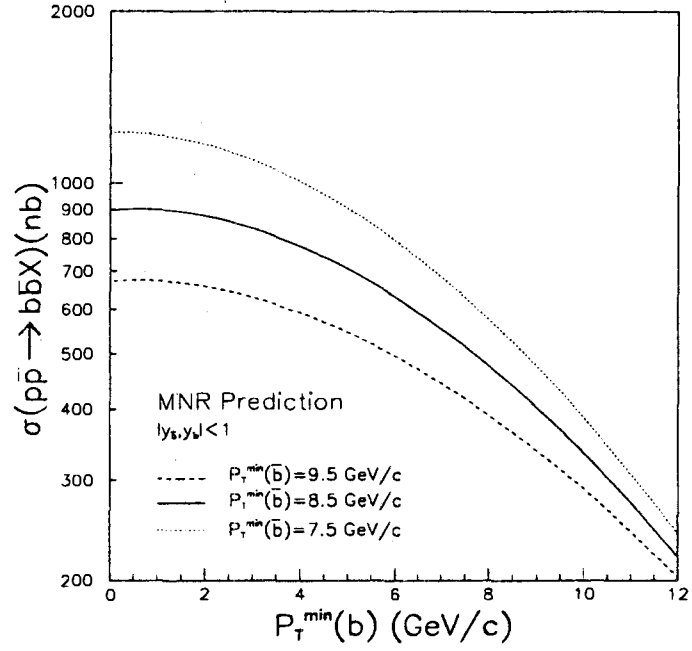


Figure 2.8: A comparison of the MNR predictions for $\sigma(p\bar{p} \rightarrow b\bar{b}X)$ for three values of $P_T^{\min}(\bar{b})$. The calculation assumes $|y_b, y_{\bar{b}}| < 1$.

Chapter 3

Experimental Apparatus

3.1 The CDF Detector

3.1.1 Introduction

The CDF detector is a general purpose 4π detector for studying $p\bar{p}$ collisions at a center-of-mass energy of 1.8 TeV. An isometric view of the detector is shown in figure 3.1. The detector is cylindrically symmetric about the beam axis and is composed of the movable central detector and the stationary forward and backward detectors. Figure 3.2 shows a cross section of the forward and central detectors. The forward and backward detectors are identically instrumented with gas-sampling electromagnetic and hadronic calorimeters and a muon system utilizing magnetized steel toroids for momentum measurement. The central detector is divided into central and plug regions. The central region of the central detector is instrumented with drift chambers for vertex determination and particle tracking. A superconducting solenoid encasing the drift chambers enables measurement of charged particle momenta. Surrounding the solenoid are scintillator-based electromagnetic and hadronic

calorimeters and muon chambers. The plug region contains electromagnetic and hadronic gas-sampling calorimeters and has partial tracking coverage. The forward/backward detectors and the plug region of the central detector were not utilized in this analysis and will not be discussed in further detail. The CDF detector is described in detail in a special edition of Nuclear Instruments and Methods [8].

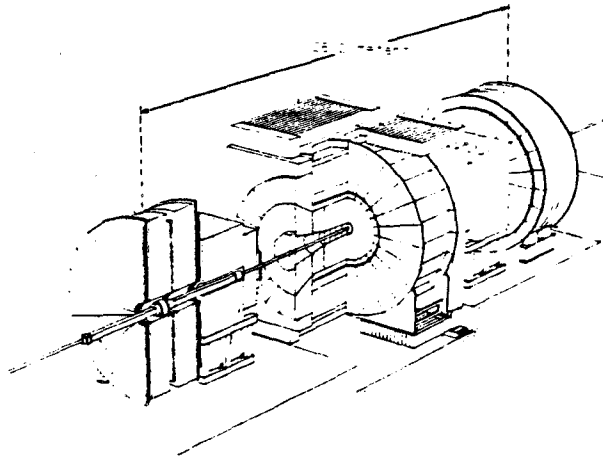


Figure 3.1: Isometric view of the CDF detector.

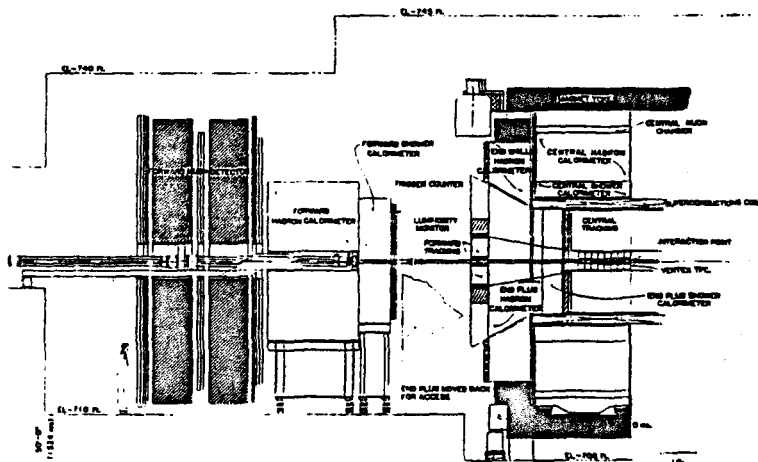


Figure 3.2: Cross section of the forward detector and a portion of the central detector.

The CDF coordinate system is defined with the positive z axis in the direction of the proton beam. The positive y axis points vertically and the positive x axis points horizontally away from the center of the Tevatron ring. The polar angle, θ , is zero along the positive z axis and the azimuthal angle, ϕ is zero along the positive x axis. It is often more convenient to speak in terms of pseudorapidity, η , than polar angle, θ . The pseudorapidity is defined as

$$\eta \equiv \ln \cot \frac{\theta}{2} = \frac{1}{2} \ln \frac{P + p_z}{P - p_z}.$$

For an energetic particle, pseudorapidity is a good approximation to the particles rapidity, y .

$$y = \frac{1}{2} \ln \frac{E + p_z}{E - p_z}.$$

Rapidity is additive under Lorentz boosts in the z direction and is thus a useful quantity in $p\bar{p}$ physics.

Starting at the interaction region and proceeding radially outward the major detector subsystems in the central region ($|\eta| \leq 1.1$) are: the Vertex Time Projection Chamber (VTPC), the Central Tracking Chamber (CTC), the Central Electromagnetic Calorimeter (CEM), the Central Hadronic Calorimeter (CHA), and the Central Muon Chambers (CMU). Each of these subsystems is described in detail below.

3.1.2 The Vertex Time Projection Chamber

The Vertex Time Projection Chamber (VTPC) is designed to provide tracking information close to the interaction region for event-by-event vertex reconstruction. The VTPC consists of eight octagonal modules placed side-by-side along the beampipe. Two modules of the

VTPC are shown in figure 3.3. Each module is composed of a central high voltage grid with a drift space on either side. Each module is capped with a proportional chamber readout consisting of sense wires and cathode pads. The readouts are segmented into octants. Charged particles traversing the VTPC volume ionize the gas filling the chambers (nominally 50-50 argon/ethane). The ionization electrons drift towards the wires and produce signals. Using the wire positions and the arrival times of the wire signals, tracks are reconstructed in the $r - z$ plane. The reconstructed tracks are parametrized in terms of their polar angle, θ and their extrapolated intersection with the z axis. Clusters of tracks with similar z intercepts are used to reconstruct primary z vertices. A typical distribution of z vertices reconstructed from VTPC information is shown in figure 3.4. The distribution is well fit by a gaussian with $\sigma = 30$ cm. The width of the gaussian is due to the longitudinal extent of the colliding proton and antiproton bunches. The VTPC is capable of reconstructing z vertices with a resolution of about 2 mm.

3.1.3 The Central Tracking Chamber

The CTC is a large volume wire chamber lying outside the volume of the VTPC and inside the superconducting solenoid. The CTC provides tracking information primarily in the $r - \phi$ plane. Figure 3.5 shows a transverse section of the CTC.

There are 84 layers of sense wires grouped into 9 "superlayers". Within each superlayer, the sense wires are further subdivided into measurement cells. Five of the superlayers contain 12 sense wires per cell, each parallel to the beam axis. These superlayers are referred to as axial superlayers and are used for the determination of track curvature in the transverse plane. The remaining four superlayers contained six wires per cell with each

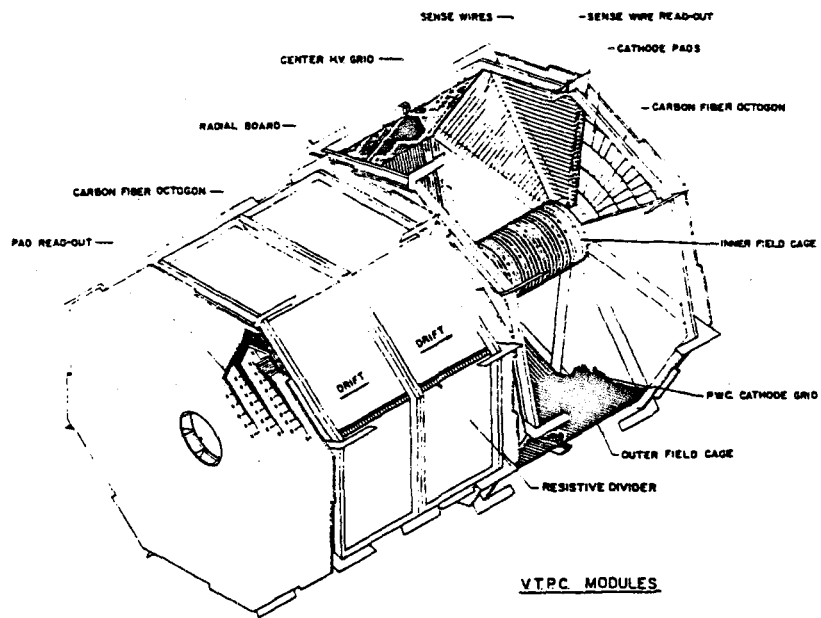


Figure 3.3: Isometric view of two VTPC modules.

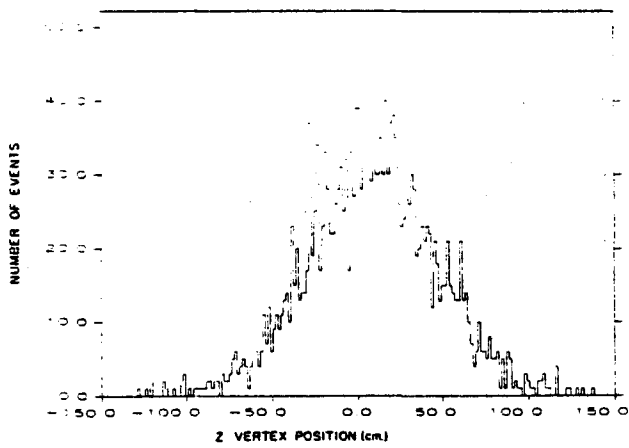


Figure 3.4: Typical distribution of z vertices from CDF events.

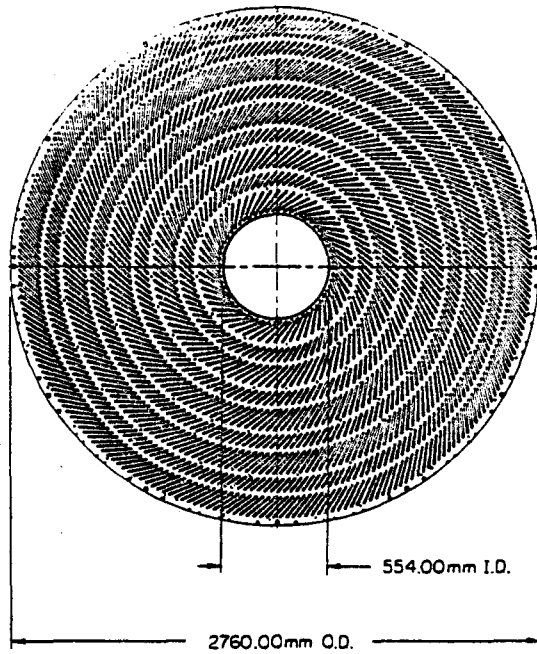


Figure 3.5: Transverse view of the Central Tracking Chamber.

superlayer having an alternating $\pm 3^\circ$ angle with respect to the beam axis. These layers are referred to as stereo superlayers and provide information about the polar angle of the tracks. The axial and stereo superlayers alternate, with the inner and outermost superlayers being axial. Each cell in every superlayer was tilted 45° with respect to the radial direction. This tilt compensates for the Lorentz force upon the drift electrons due to the solenoidal magnetic field, yielding approximately azimuthal drift trajectories that greatly simplify the drift time-to-distance relationship. The axial position resolution for each layer is better than 200μ and the z resolution is about 1 mm.

Due to the solenoidal magnetic field, charged particles follow helical trajectories within the CTC volume. The trajectories are parametrized by the following five quantities:

- c - The half-radius of curvature. The P_T of a track is given by the relation

$$P_T = \frac{0.000149898B}{c} \text{ GeV}$$

where B is the magnitude of the solenoidal field in Tesla.

- d_0 - The distance of closest approach of the track to the origin in the $r - \phi$ plane.
- ϕ_0 - The azimuthal angle of the track at the point of closest approach to the origin.
- z_0 - The z position of the track at the point of closest approach of the track to the origin.
- $\cot \theta$ - the cotangent of the polar angle of the track at the point of closest approach of the track to the origin.

For isolated tracks, the rms transverse momentum resolution of the CTC is given by

$$\frac{\delta P_T}{P_T} = 0.0020 P_T$$

where P_T is expressed in GeV. The outermost superlayer of the CTC covers the region $|\eta| < 1$. Particles traversing the CTC at greater values of η pass through fewer superlayers with a corresponding degradation of tracking performance.

3.1.4 The Central Calorimetry

The central calorimetry covers the region $|\eta| < 1.1$ and is composed of an electromagnetic calorimeter (CEM) followed by a hadron calorimeter (CHA). The central calorimetry forms a barrel around the solenoid and is divided into 48 wedge-shaped modules. Each wedge subtends 15° in ϕ and 1.1 units in η . Each wedge is a sandwich of lead-scintillator for the CEM followed by an iron-scintillator sandwich that forms the CHA. Within each wedge, the sampling medium is subdivided into 10 sections in η , so that the $\delta\eta \times \delta\phi$ tower segmentation is $0.11 \times 15^\circ$. The CEM portion of a wedge is shown in figure 3.6. The tower structure is evident in the figure; note that the towers are projective, that is, point to the nominal interaction region. Light from the scintillators is brought out through light pipes at the ϕ boundaries of the wedge to photomultiplier tubes.

Each wedge of the CEM has a gas proportional chamber (CES) embedded at the approximate shower maximum position (nominally $5.9 X_0$). The chambers are read out with orthogonal sets of anode wires and cathode strips. The wires provide a ϕ view and the strips yield a profile of the shower in z . The much finer segmentation of the CES with respect to

the CEM allows a more precise measurement of the transverse shower shape and position.

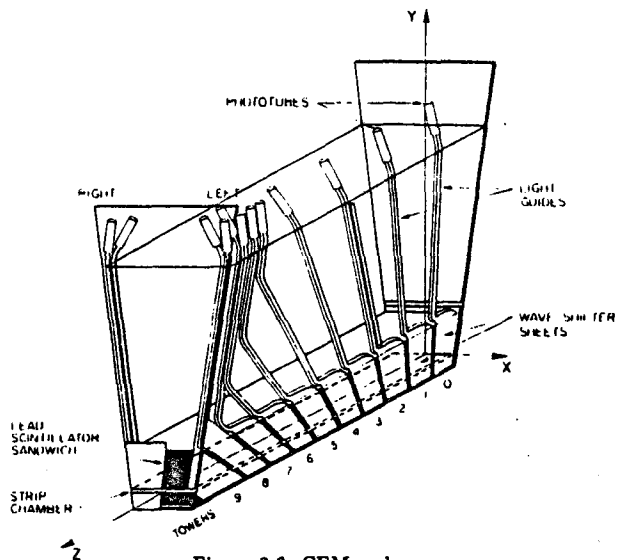


Figure 3.6: CEM wedge.

3.1.5 The Central Muon Chambers

The Central Muon Chambers (CMU) are located behind the CHA. The CMU provides muon identification for $|\eta| < 0.63$. Figure 3.7 shows the position of the chambers in a wedge. There are three chambers per wedge with each chamber containing 16 drift cells. A cross section of a single muon chamber is shown in figure 3.8. Each of the four layers of drift cells has only two electronic channels for readout as alternate sense wires are ganged together. ϕ information is reconstructed from drift times and z information from charge division. The chamber resolution in the ϕ direction is $250 \mu\text{m}$ and 1.2 mm in the z direction.

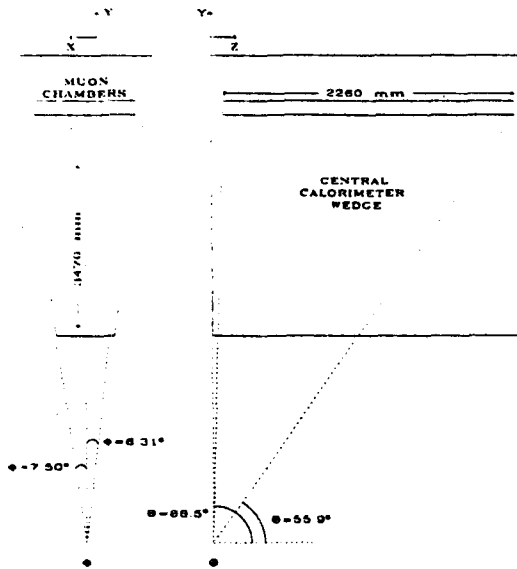


Figure 3.7: Location of the Central Muon Chambers in a wedge.

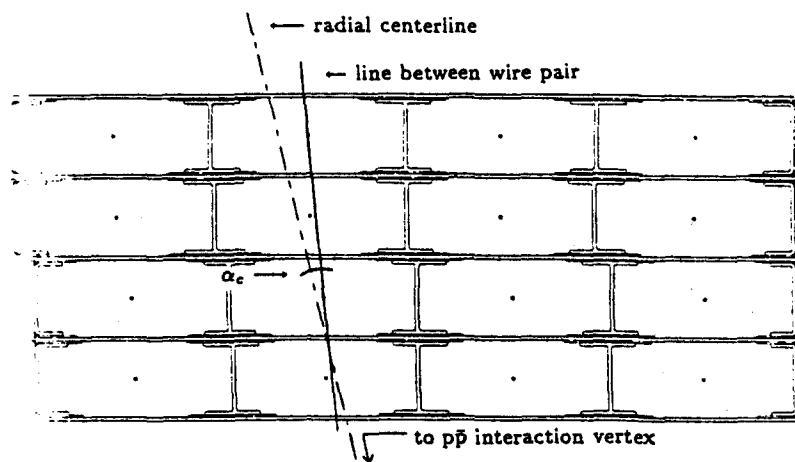


Figure 3.8: Cross section in the $r - \phi$ plane of one CMU chambers showing the 16 drift cells.

3.1.6 The Trigger System

The Tevatron was operated during the 1988-89 run with six bunches of protons and six bunches of antiprotons in the machine. One pair of bunches intersected at the CDF interaction region every 3.5 μ seconds. The total inelastic cross section at 1.8 TeV is approximately 50 mb, yielding a rate of 50 kHz for a typical luminosity of $1 \times 10^{30} \text{ cm}^{-2}\text{s}^{-1}$. The rate at which events could be written to tape was only about 1 Hz. A multilevel trigger system was built in order to rapidly decide whether an event was of interest. At each level of the trigger, the event rate was progressively reduced by the imposition of progressively more sophisticated requirements.

The lowest level of the trigger, level 0, selected inelastic collisions by requiring simultaneous hits in scintillating paddles located in front of the forward and backward detectors. Once the level 0 trigger was satisfied, data-taking was inhibited during the next beam crossing, allowing 7 μ s for level 1 to make a decision.

The level 1 and 2 trigger decisions were based upon information from the calorimeters, the muon chambers, and a fast hardware tracker (the CFT). The trigger gangs together two calorimeter towers into a single "trigger tower". A trigger tower has a segmentation in $\delta\eta \times \delta\phi$ of $0.2 \times 15^\circ$. The level 1 trigger looks for individual trigger towers in excess of a programmable threshold. It may also make decisions based upon the presence of stiff tracks in the CTC or the muon chambers. The level 2 trigger is capable of associating the energy clusters, CTC and muon tracks, used individually in level 1, with each other in order to make decisions based on more global event properties. The typical time to make a level 2 decision was approximately 100 μ s. Once the level 2 trigger was satisfied, the readout of

the detector was initiated; readout of all 100,000 channels typically took 10-15 ms.

The data read out of the detector was digitized and buffered for further processing by the level 3 trigger. The level 3 trigger consisted of FORTRAN-77 programs running on Advanced Computer Program (ACP) processors located in VME crates, allowing sophisticated event filtering. Once passed by level 3, an event was recorded on magnetic tape.

Chapter 4

Electron Identification

Electron identification was divided into two stages. The first stage entailed the identification of electron “candidates”. Electron candidates are collections of signals in the detector which may have been generated by an electron. The second stage consisted of the imposition of various selection criteria to improve the rejection of backgrounds.

4.1 Identification of Electron Candidates

The selection of an electron candidate began with the examination of the energy deposition in the Central Electromagnetic Calorimeter (CEM). The transverse energy¹, E_T , associated with each tower of the CEM was calculated from the energy deposited in that tower and the position of the tower center. Clusters were then formed by associating towers on the basis of their relative positions and their E_T . The electron clustering algorithm first looked for towers that had an E_T above a 3 GeV threshold; these towers were called seed towers.

¹ $E_T \equiv E \sin\theta$

The algorithm looked next at the towers adjacent to each seed tower at higher and lower values of η . If an adjacent tower had E_T above 0.1 GeV then that tower (a “shoulder” tower) was added to the cluster. Note that a cluster was limited to a maximum of three towers, a seed and two shoulders, and that each tower of the cluster was in the same ϕ wedge. The cluster E_T was defined as the scalar sum of the E_T of each tower participating in the cluster. A sum was also made of the transverse hadronic energy associated with the clustered towers. The quantity, HAD/EM , was defined to be the ratio of the transverse electromagnetic energy, E_T^{EM} , and the transverse hadronic energy, E_T^{HAD} . Clusters with $E_T^{EM} > 5$ GeV and $HAD/EM < 0.125$ were considered to be electron candidates.

4.2 Electron Quality Variables

4.2.1 LSHR

One method of rejecting electron background is to compare the transverse shape of an electron shower with that for the background, using the tower segmentation of the CEM. A typical CEM tower is 25×46 cm². An electron in the CEM has a transverse shower size of a few centimeters, meaning that an electron is well contained by a single tower, depositing little or no energy in the adjacent towers. Overlapping photons and charged hadrons are a major source of electron background. Overlaps are most likely to occur inside of jets which have a large transverse extent. Overlaps are then likely to be associated with other particles that will deposit energy in adjacent towers. Background due to overlaps may be rejected by comparing the observed energy deposition to that expected for an electron. Test beam measurements have been made to determine the energy deposited by an electron in towers

adjacent to the one struck as a function of the point at which the electron impacted the primary tower. This information is used to define the variable LSHR:

$$\text{LSHR} = 0.14 \sum_i \frac{M_i - P_i}{\sqrt{0.14^2 E + (\Delta P_i)^2}}.$$

M_i is the energy deposited in an adjacent tower, P_i is the predicted energy deposition in that tower from the test beam measurements, ΔP_i is the error in P_i associated with a 1 cm variation in the impact point. E is the electromagnetic energy of the cluster.

4.2.2 CES χ^2

LSHR uses the CEM tower segmentation to compare the transverse shower shape to that expected for an electron. The strip chamber may be used in a similar manner. The segmentation of the strip chambers is much finer than that of the CEM and is therefore useful in rejecting background events in which the jet has fragmented to a few, collimated particles or in which the overlapping particles are well separated from the rest of the jet. The strip chambers are embedded in the CEM at approximately shower maximum. The transverse extent of an electron shower at this distance is such that greater than 99% of the shower is contained in 11 strip channels, allowing for a reasonable determination of the shower profile. A standard electron strip profile was obtained through test beam measurements. A least-squares fit of the standard profile to the measured profile was performed and the χ^2 was defined as

$$\chi^2 = \frac{1}{4} \sum_{i=1}^{11} \frac{(m_i - p_i)^2}{\sigma_i^2},$$

where i is the channel index, m_i is the measured profile, and p_i is the standard profile. Both measured and standard profiles were normalized to unity. The variance, σ_i^2 , is the squared RMS fluctuation of CES channel i in the measured, unity normalized strip profile. The channel variance as a function of channel response was determined from test beam measurements using 10 GeV electrons. The normalized variance of the normalized strip profile for 10 GeV electrons was found to be

$$\sigma_{10,i}^2 = (0.026)^2 + p_i(0.096)^2.$$

The variance of a channel is proportional to the number of secondaries passing through that channel which, in turn, is dependent upon the point at which the shower evolution is sampled. Since the shower evolution has a logarithmic dependence upon the energy of the primary, E , the variance is expected to depend weakly upon the electron energy. This weak dependence is parametrized from testbeam measurements as

$$\sigma_i^2 = \sigma_{10,i}^2 \left(\frac{10}{E} \right)^{0.747},$$

where E is the primary electron energy in GeV. The determination of the standard profiles and the calculation of the CES χ^2 is discussed in detail in reference ??.

4.2.3 Fiducial Cuts

In order to assure proper measurement of the electron shower, certain regions of the CEM were excluded from consideration. The electron was required to be in the fiducial region defined as follows:

$|\Delta\phi| < 21.5$ cm from the tower center, 9 cm $< |z| < 200$ cm.

The fiducial cuts ensure that the shower is well away from the ϕ cracks between CEM wedges, away from the 90° crack between the East and West arches and that the electron does not extend beyond adequate CEM coverage in $|\eta|$. The strip chamber was used to determine the electron position for the purposes of determining fiduciality.

4.2.4 Track Matching

Variables such as LSHR and the CES χ^2 provide electron background rejection based upon a comparison of the electromagnetic energy deposition with what is expected for electrons. The association of a track with the EM energy deposition is usually required in electron reconstruction and provides another method for rejecting overlap events. The position of the EM shower centroid may be accurately determined by the strip chambers and compared to the propagated track position. An electron is expected to leave a track that matches well with its strip chamber profile in both the $r\phi$ and z views. An overlap event is expected to have a poorer match between the track and the EM shower centroid because they are not produced by the same particle.

4.2.5 HAD/EM

Electromagnetic showers develop more rapidly than hadronic showers as a function of the amount of material traversed; this fact is exploited to allow simultaneous measurements of the electromagnetic and hadronic energy depositions in the same calorimetry tower. The central electromagnetic calorimeter (CEM) is positioned in front (*i.e.* closer to the interaction region) of the central hadronic calorimeter (CHA). Electromagnetic showers

develop in the CEM and are usually well contained within the volume of that calorimeter. Hadronic showers do not typically develop until a particle reaches the CHA, leaving a minimum ionizing trail in the CEM. Electromagnetic showers may be distinguished from hadronic showers by comparing the energy deposition in the CEM to that in the CHA. The HAD/EM variable is defined as the ratio of the energy deposited into the hadronic compartments of the towers forming an electron cluster to the energy deposited into the electromagnetic compartments.

Chapter 5

Muon Identification

Muon identification was divided into two stages. The first stage entailed the identification of muon “candidates”. Muon candidates are collections of signals in the detector which may have been generated by a muon. The second stage consisted of the imposition of various selection criteria to improve the rejection of muon backgrounds.

5.1 Identification of Muon Candidates

The primary tool for the detection of muons in the central region ($|\eta| < 1$) of CDF is the central muon (CMU) system. The CMU system has been described in chapter 3; for the purposes of the following discussion it is necessary only to recall that the system consists of four layers of wire chambers, positioned behind the calorimetry, that allow the reconstruction of muon tracks (“stubs”) with a resolution of $250 \mu\text{m}$ in $r\phi$ and 1.2 mm in z . A muon stub was considered a candidate muon if there was a CTC track that matched the $r\phi$ position of the stub to within 10 cm .

5.2 Muon Quality Variables

5.2.1 Fiducial Cuts

Muon fiducial cuts were imposed in order to guarantee that the portions of the muon chambers in use were fully efficient and that the CTC would also be efficient for the reconstruction of the muon track.

5.2.2 Track-Stub Matching

To perform a precision matching of a stub to a CTC track, the effects of multiple Coulomb scattering in the volume of the calorimetry had to be considered. A muon traversing a slab of material will undergo multiple scatterings off of the atoms comprising the material. The scattering is described by an angle, θ , which is defined as the angular difference in the momentum of the muon at incidence and at a distance, L , into the material. The distribution of θ is roughly gaussian with a width, θ_0 , given by [10]

$$(5.1) \quad \theta_0 = \frac{13.6\text{MeV}/c}{\beta p} Z_{inc} \sqrt{L/L_R [1 + 0.038/\ln(L/L_R)]},$$

where β , p , Z_{inc} are the velocity, momentum, and charge number of the incident particle and (L/L_R) gives the number of radiation lengths traversed by the particle.

The matching of a track and stub was described in terms of the quantities $\Delta(r\phi)$ and Δz , which are the differences in the $r\phi$ and z values at which the CTC track and the muon stub intercept the front face of the muon chambers. Utilizing the above expression for θ_0 and the Bethe-Bloch formula for energy loss, a software routine was written to calculate the expected distributions of $\Delta(r\phi)$ and Δz , given a sample of muons [11]. The standard deviations of

the distributions were used to calculate the significances: $\Delta(r\phi)/\sigma_{\Delta(r\phi)}$, $\Delta z/\sigma_{\Delta z}$. A CTC track and CMU stub were considered to match if the $\Delta(r\phi)$ and Δz significances were less than three.

5.2.3 Vertex Matching

The matching of CTC tracks to the event vertex is useful for reducing background from the underlying event. Tracks associated with the hard scattering originate from a common vertex. The underlying event is due to the relatively soft interactions between the remaining partons. Tracks produced by the underlying event have a flat distribution in η . The matching of the track to the vertex in the $r - \phi$ plane is measured by the distance of closest approach (DCA), which is the perpendicular distance from the track to the origin at the point at which the track come closest to the vertex. The matching of a track to the vertex in z is measured simply by the difference in the z coordinate of the vertex and the z coordinate of the track at the distance of closest approach.

5.2.4 Energy Deposition

A muon signature may be faked by energetic hadrons when some of the hadronic shower leaks from the back of the calorimeter and creates a stub in the muon chambers. This background may be reduced by propagating the muon CTC track to the face of the electromagnetic and hadronic calorimeters and requiring that the energy deposited in those towers be consistent with a minimum ionizing particle.

Chapter 6

Analysis

6.1 The Electron-Muon Data Sets

The data used in this analysis originated from the ELECTRON.EMC.5.CMU.3 trigger. The requirements of the trigger are detailed in 6.6.2. The trigger required a central electron candidate with $E_T > 5$ GeV and a central muon candidate with $P_T > 3$ GeV/c. Two samples were culled from these events: the “analysis” data set and the “unbiased” data set.

6.1.1 The Analysis $e\mu$ Data Set

The requirements used to select the events in the analysis data set are listed in table 6.1.1. The quantities shown in the table are discussed in chapters 4 and 5. The $b\bar{b}$ content of this sample was determined in order to measure the $b\bar{b}$ production cross section.

6.1.2 The Unbiased $e\mu$ Data Set

The unbiased data set comprised events satisfying the following requirements:

Electron Requirements	Muon Requirements
$E_T > 5 \text{ GeV}$ $HAD/EM \leq 0.05$ $E/P \leq 1.4$ $LSHR < 0.2$ $ \Delta(r\phi) \leq 1.5 \text{ cm}$ $ \Delta(z) \leq 2.5 \text{ cm}$ Strip $\chi^2 \leq 10$ Only 1 3D track FIDELE	$P_T > 3 \text{ GeV}/c$ Track-stub match in x and $z \leq 3\sigma$ Track DCA $< 50 \text{ mm.}$ z of track $< 5 \text{ cm.}$ from vertex $< 2 \text{ GeV}$ EM energy in μ tower $< 4 \text{ GeV}$ HAD energy in μ tower FIDCMU
Event Requirements	
Missing E_T significance < 2.4 $ z_{\text{vertex}} < 60 \text{ cm.}$ Invariant mass of $e\mu$ pair $> 5 \text{ GeV}/c^2$	

Table 6.1: The requirements used in creating the analysis $e\mu$ data set. The quantities are defined in chapters 4 and 5.

- A muon candidate with $P_T > 3.0 \text{ GeV}$ and track-stub matching in the xy and zy planes within 3.5σ of that expected for a muon undergoing multiple scattering and
- An electron candidate with $E_T > 4.0 \text{ GeV}$ that is associated with at least one track.

This data set was used to determine the efficiencies of the analysis data set selection requirements for $b\bar{b}$ events; details are located in section 6.4.

6.2 Method

6.2.1 Sources of Electron-Muon Pairs

The $e\mu$ data are primarily comprised of events from: $b\bar{b}$ production, $c\bar{c}$ production, ‘fakes’, and the sequential decay of single b quarks.

Bottom Decays

Leptons from bottom decays may be direct ($b \rightarrow \ell \nu$) or indirect ($b \rightarrow cX, c \rightarrow \ell X$).

In the absence of $B^0 \bar{B}^0$ mixing, two direct leptons ($b \rightarrow \ell^- X, \bar{b} \rightarrow \ell^+ Y$) or two indirect leptons ($b \rightarrow cX \rightarrow \ell^+ X, \bar{b} \rightarrow \bar{c}Y \rightarrow \ell^- Y$) would always have charges of opposite sign (OS), whereas one direct lepton ($b \rightarrow \ell^- X$) and one indirect lepton ($\bar{b} \rightarrow \bar{c}Y \rightarrow \ell^- Y$) would have charges of the same sign (SS).

An electron-muon pair may also come from the sequential decay of a single bottom quark ($b \rightarrow \ell^- c\nu, c \rightarrow \ell^+ s\nu$). Such pairs are always of opposite sign. Sequential decays were removed from the data by demanding that the $e\mu$ invariant mass be greater than 5 GeV.

Charm Decays

The dual semileptonic decay of a pair of directly produced charm quarks can also lead to an electron and a muon in the final state

$$p\bar{p} \rightarrow c\bar{c} \rightarrow e\mu X$$

As there is negligible mixing, the leptons will always be of opposite sign. The contribution from $c\bar{c}$ is expected to be small relative to that from $b\bar{b}$ since the P_T spectrum of leptons from $c\bar{c}$ is much softer than that for leptons from $b\bar{b}$.

Fakes

Events may also be composed of electrons or muons that are of non-prompt origin or are misidentified particles. Example of leptons from non-prompt sources are electrons from photon conversions and muons from decays-in-flight. Muon and electron signatures in the detector may be produced by other particles or combinations of other particles. A particle which does not shower in the calorimetry may reach the muon chambers and be misidentified as a muon. Overlapping π^0 's and charged pions may be misidentified as an electron. Non-prompt or misidentified particles will be referred to as 'fakes' and events in which one or both of the leptons are fake will be referred to as fake events. Since the processes which produce fake electrons and muons are random with respect to the charge of the fake produced, fake events are equally likely to have $e\mu$ pairs of opposite sign or same sign.

6.2.2 The Method for Measuring $\sigma(b\bar{b}X)$

This thesis presents the measurement of the cross section for $b\bar{b}$ production from events containing electron-muon pairs. To explicitly indicate the stage in the data analysis to which quantities refer, the following convention for superscripts has been used:

- (⁰) refers to all events produced in an integrated luminosity, \mathcal{L} .
- (¹) refers to the events in which an $e\mu$ pair satisfied the trigger. This is the unbiased $e\mu$ data set.
- (²) refers to the events in which an $e\mu$ satisfies all the selection requirements. This is the analysis $e\mu$ data set.

The cross section for inclusive $b\bar{b}$ production, $\sigma(b\bar{b}X)$, is related to the number of produced $b\bar{b}$ events, $N_{b\bar{b}}^{(0)}$, via

$$(6.1) \quad \sigma(b\bar{b}X) = \frac{N_{b\bar{b}}^{(0)}}{\mathcal{L}},$$

where \mathcal{L} is the integrated luminosity. Again, $N_{b\bar{b}}^{(0)}$ is the number of $b\bar{b}$ pairs that have been produced, not the number finally observed in the analysis. No b decay mode has been specified at this point; no trigger requirements or event selection cuts have been imposed.

The number of $b\bar{b}$ events that satisfy the $e\mu$ trigger requirements, $N_{b\bar{b}}^{(1)}$, is obtained from the total number of $b\bar{b}$ events produced, $N_{b\bar{b}}^{(0)}$, by the application of the branching fraction for $b\bar{b} \rightarrow e\mu X$, B , the acceptance of the detector to $e\mu$ pairs, A , and the efficiency of the trigger, ϵ_{trig} :

$$(6.2) \quad N_{b\bar{b}}^{(1)} = N_{b\bar{b}}^{(0)} B A \epsilon_{trig}.$$

In a real experiment, the number of observed $e\mu$ pairs will not necessarily equal the number of observed $b\bar{b}$ events as there may also be contributions from $c\bar{c}$ production and fakes. The number of $e\mu$ events passing all analysis cuts, $N_{e\mu}^{(2)}$, is related to the number of $b\bar{b}$ events passing all cuts, $N_{b\bar{b}}^{(2)}$, by

$$(6.3) \quad N_{e\mu}^{(2)} = N_{b\bar{b}}^{(2)} + N_{c\bar{c}}^{(2)} + F^{(2)},$$

where $N_{c\bar{c}}^{(2)}$ is the contribution from $c\bar{c}$ production, and $F^{(2)}$ is the contribution from fakes.

The contribution from the fakes may be eliminated by noting that fake events are equally likely to be of opposite sign or same sign. Separating the data into opposite sign and same

sign contributions gives,

$$N_{e\mu}^{OS(2)} = N_{bb}^{OS(2)} + N_{cc}^{(2)} + \frac{1}{2}F^{(2)},$$

$$N_{e\mu}^{SS(2)} = N_{bb}^{SS(2)} + \frac{1}{2}F^{(2)}.$$

It is seen that the fake contribution subtracts out in taking the difference of the opposite sign and same sign $e\mu$ events:

$$(6.4) \quad N_{e\mu}^{OS(2)} - N_{e\mu}^{SS(2)} = N_{bb}^{OS(2)} - N_{bb}^{SS(2)} + N_{cc}^{(2)}.$$

Defining $\Delta_{e\mu}^{(2)}$ as the number of excess opposite sign $e\mu$ events and $\Delta_{bb}^{(2)}$ as the number of excess opposite sign $b\bar{b}$ events, equation 6.4 may be written:

$$(6.5) \quad \Delta_{e\mu}^{(2)} = \Delta_{bb}^{(2)} + N_{cc}^{(2)}.$$

Event-by-event separation of $b\bar{b}$ and $c\bar{c}$ contributions is not possible with the inclusive $e\mu$ decay mode. A statistical separation is possible, however, and allows the determination of the fraction of $e\mu$ events due to $b\bar{b}$. Defining $f_{bb}^{(2)}$ as the fraction of the sign-subtracted $e\mu$ events due to $b\bar{b}$ production,

$$(6.6) \quad \Delta_{bb}^{(2)} = f_{bb}^{(2)} \Delta_{e\mu}^{(2)}.$$

$\Delta_{b\bar{b}}^{(2)}$ is related to $\Delta_{b\bar{b}}^{(1)}$ through the efficiency of the selection cuts:

$$(6.7) \quad \epsilon_{cuts} \equiv \frac{\Delta_{b\bar{b}}^{(2)}}{\Delta_{b\bar{b}}^{(1)}}.$$

The number of excess opposite sign $b\bar{b} \rightarrow e\mu X$ events satisfying the trigger is then

$$(6.8) \quad \Delta_{b\bar{b}}^{(1)} = \frac{f_{b\bar{b}}^{(2)} \Delta_{e\mu}^{(2)}}{\epsilon_{cuts}}.$$

To arrive at a cross section, it is necessary to obtain the total number of $b\bar{b} \rightarrow e\mu X$ events that triggered. This number is calculable from the number of excess opposite sign events, $\Delta_{b\bar{b}}^{(1)}$, through various branching fractions and lepton acceptances. Defining $f_{surv}^{(1)}$ as the fraction of triggered $b\bar{b}$ events surviving the sign-subtraction

$$(6.9) \quad N_{b\bar{b}}^{(1)} = \frac{\Delta_{b\bar{b}}^{(1)}}{f_{surv}^{(1)}}.$$

Using equation 6.8,

$$(6.10) \quad N_{b\bar{b}}^{(1)} = \frac{f_{b\bar{b}}^{(2)} \Delta_{e\mu}^{(2)}}{f_{surv}^{(1)} \epsilon_{cuts}}.$$

Thus, the observed excess of opposite sign $e\mu$ pairs is related to the total number of $b\bar{b}$ events satisfying the trigger. The number of $b\bar{b}$ events created is obtained from equation 6.2:

$$(6.11) \quad N_{b\bar{b}}^{(0)} = \frac{f_{b\bar{b}}^{(2)} \Delta_{e\mu}^{(2)}}{f_{surv}^{(1)} \epsilon_{cuts} B A \epsilon_{trig}}.$$

Substituting into equation 6.1 yields

$$(6.12) \quad \sigma(b\bar{b}X) = \frac{f_{b\bar{b}}^{(2)} \Delta_{e\mu}^{(2)}}{f_{surv}^{(1)} \epsilon_{cuts} \mathcal{B} \mathcal{A} \epsilon_{trig} \mathcal{L}}.$$

The remainder of this chapter describes the evaluation of each term in the above expression. The calculation of $f_{surv}^{(1)}$ is detailed in section 6.2.3; the calculation of the event selection efficiency, ϵ_{cuts} , is detailed in section 6.4; the trigger efficiency, ϵ_{trig} is discussed in section 6.6.2; the determination of the $b\bar{b}$ fraction, $f_{b\bar{b}}^{(2)}$, is detailed in section 6.3; the lepton acceptance, \mathcal{A} , is calculated in section 6.5. The comparison of the results with the theoretical expectation is discussed in section 6.7.

6.2.3 The Survival Fraction $f_{surv}^{(1)}$

$f_{surv}^{(1)}$ was defined as the fraction of $b\bar{b}$ events surviving the subtraction of the same sign events from the opposite sign events:

$$(6.13) \quad f_{surv}^{(1)} = \frac{N_{b\bar{b}}^{OS(1)} - N_{b\bar{b}}^{SS(1)}}{N_{b\bar{b}}^{(1)}}.$$

In the absence of $B^0\bar{B}^0$ mixing, $N_{b\bar{b}}^{OS(1)}$ and $N_{b\bar{b}}^{SS(1)}$ can be written in terms of branching fractions and lepton acceptances:

$$(6.14) \quad \begin{aligned} N_{b\bar{b}}^{OS(1)} &= [\mathcal{B}(b \rightarrow e\nu X) \mathcal{A}(be) \mathcal{B}(b \rightarrow \mu\nu X) \mathcal{A}(b\mu) \\ &+ \mathcal{B}(b \rightarrow c \rightarrow e\nu X) \mathcal{A}(bce) \mathcal{B}(b \rightarrow c \rightarrow \mu\nu X) \mathcal{A}(bc\mu)] N_{b\bar{b}}^{(0)}, \\ N_{b\bar{b}}^{SS(1)} &= [\mathcal{B}(b \rightarrow e\nu X) \mathcal{A}(be) \mathcal{B}(b \rightarrow c \rightarrow \mu\nu X) \mathcal{A}(bc\mu) \end{aligned}$$

$$(6.15) \quad + \mathcal{B}(b \rightarrow c \rightarrow e\nu X)A(bce)\mathcal{B}(b \rightarrow \mu\nu X)A(b\mu)] N_{\bar{b}\bar{b}}^{(0)}.$$

$\mathcal{B}(b \rightarrow \ell\nu X)$ is the branching fraction for b producing a direct lepton, while $\mathcal{B}(b \rightarrow c \rightarrow \ell\nu X)$ is the branching fraction for b producing an indirect lepton. Likewise, $A(b\ell)$ and $A(bc\ell)$ are the acceptances for direct and indirect leptons from b decay. $B^0\bar{B}^0$ mixing modifies the above results. The probability of bottom quark mixing is given by the mixing parameter, χ , defined as

$$(6.16) \quad \chi \equiv \frac{\text{Prob}(b \rightarrow \bar{B}^0 \rightarrow B^0 \rightarrow \ell^+)}{\text{Prob}(b \rightarrow \bar{B} \rightarrow \ell^\pm)},$$

where B^0 refers to either B_d^0 or B_s^0 and B represents any bottom flavored hadron. The probability of one quark, both quarks, or neither quarks mixing is

$$\begin{aligned} 2\chi(1-\chi) & \text{ One quark mixes,} \\ \chi^2 & \text{ Both quarks mix,} \\ (1-\chi)^2 & \text{ Neither quarks mix.} \end{aligned}$$

Including $B^0\bar{B}^0$ mixing, the equations in 6.14 are now

$$(6.17) \quad \begin{aligned} N_{\bar{b}\bar{b}}^{OS(1)} &= \{[P_{bc}P_{b\mu} + P_{bcc}P_{bc\mu}][\chi^2 + (1-\chi)^2] \\ &+ [P_{bc}P_{bc\mu} + P_{bcc}P_{b\mu}]2\chi(1-\chi)\} N_{\bar{b}\bar{b}}^{(0)}, \end{aligned}$$

$$(6.18) \quad \begin{aligned} N_{\bar{b}\bar{b}}^{SS(1)} &= \{[P_{bc}P_{b\mu} + P_{bcc}P_{bc\mu}][2\chi(1-\chi)] \\ &+ [P_{bc}P_{bc\mu} + P_{bcc}P_{b\mu}][\chi^2 + (1-\chi)^2]\} N_{\bar{b}\bar{b}}^{(0)}, \end{aligned}$$

where the compact notation $P_{b\ell} \equiv B(b \rightarrow e\nu X)A(b\ell)$ has been used. Substituting into equation 6.13 gives

$$(6.19) \quad f_{surv}^{(1)} = \frac{[P_{bc}P_{b\mu} + P_{bcc}P_{bc\mu} - P_{be}P_{bc\mu} - P_{bcc}P_{b\mu}](1 - 2\chi)^2}{[P_{bc}P_{b\mu} + P_{bcc}P_{bc\mu} + P_{be}P_{bc\mu} + P_{bcc}P_{b\mu}]}$$

Dividing top and bottom by $P_{bc}P_{b\mu}$ and defining

$$\gamma_\ell \equiv \frac{B(b \rightarrow c \rightarrow \ell\nu X)}{B(b \rightarrow \ell\nu X)},$$

$$\alpha_\ell \equiv \frac{A(bc\ell)}{A(b\ell)},$$

equation 6.13 becomes

$$(6.20) \quad f_{surv}^{(1)} = \frac{(1 - \alpha_e\gamma_e)(1 - \alpha_\mu\gamma_\mu)}{(1 + \alpha_e\gamma_e)(1 + \alpha_\mu\gamma_\mu)}$$

The values of $\gamma(\ell)$ were calculated from known branching ratios [16]. $\gamma(e)$ and $\gamma(\mu)$ were found to be 0.88 ± 0.15 and 0.92 ± 0.16 , respectively.

The determination of α_ℓ is given in section 6.5.

6.3 Determining $f_{b\bar{b}}$

The fraction of the sign-subtracted $e\mu$ events due to $b\bar{b}$ production, $f_{b\bar{b}}$, was determined from the lepton P_T^{rel} distribution. P_T^{rel} is defined as the component of the lepton momentum transverse to the axis of the associated jet (figure 6.1). The data were fitted with the sum of the normalized b and c P_T^{rel} distributions from Monte Carlo, with the free parameter of the fit being $f_{b\bar{b}}$.

6.3.1 The Relative Transverse Momentum P_T^{rel}

Semileptonic b and c decays produce a lepton and a neutrino in association with other decay products. The lepton was identifiable in the detector. The neutrino was not directly observable and was ignored. The remaining charged decay products were identified as tracks in the CTC and were clustered together into a ‘jet’. The remaining uncharged decay products were ignored.

6.3.2 Jet Clustering

Jets are reconstructed by associating or ‘clustering’ tracks according to the distance between them. Distance is measured in terms of ΔR , the displacement in $\eta\phi$ space¹,

$$(6.21) \quad \Delta R^2 = \Delta\phi^2 + \Delta\eta^2,$$

where $\Delta\phi$ and $\Delta\eta$ are the differences in the ϕ and η coordinates of the tracks, respectively. The first stage in clustering was the selection of ‘seed’ tracks. A seed track was defined

¹See chapter 3 for the definitions of η and ϕ

as a track with $P_T > P_T^{seed}$. The seed tracks were looped over and any two seeds with $\Delta R < R_{cluster}$ were merged into a single seed by summing their momenta vectorially, where 1.0 was the nominal value of $R_{cluster}$. This process was iterated until no new mergings occurred. The second phase of clustering was the selection of all remaining, non-seed, tracks with $P_T > 400$ MeV/c. Tracks below this threshold are not reliably reconstructed by the CTC tracking algorithm. In the final phase, the selected tracks were merged with the seeds if $\Delta R < R_{cluster}$ for a seed-track pair. The jet with the smallest displacement in ΔR relative to the lepton was used to calculate the lepton P_T^{rel} . Tracks corresponding to the electron and muon were excluded from clustering.

6.3.3 Monte Carlo Distributions

The predicted shapes of the P_T^{rel} spectra for leptons from bottom and charm decays were obtained from Monte Carlo. Two event generators were used: Isajet and Single-b. Isajet generated events with a $b\bar{b}$ or $c\bar{c}$ pair and included an underlying event simulation. Single-b produced events with no underlying event and only a single bottom quark. The generated events were passed through a CDF detector simulation, trigger simulation, and standard reconstruction code. The simulated events were then subjected to the same selection requirements as the $e\mu$ data. The resultant P_T^{rel} distributions were parameterized using a gaussian convoluted with a Breit-Wigner. This functional form was chosen as it provided the best fit to the Monte Carlo distributions. The distribution for leptons from direct ($b \rightarrow \ell\nu c$) b decays and indirect ($b \rightarrow cX, c \rightarrow \ell\nu s$) b decays were parameterized separately. Figure 6.2 shows the fits to the Single-b direct electron distributions for three choices of jet clustering cone size: $R_{cluster} = 1.0, 0.7, 0.4$ and two values of the seed track P_T threshold:

$P_T^{seed} = 1.0, 0.4 \text{ GeV}/c$. Figure 6.3 shows the fits to the Single-b indirect electron distributions. The fits to the Isajet direct and indirect distributions are shown in figures 6.4 and 6.5, for the same choices of $R_{cluster}$ and P_T^{seed} listed above. Both generators reproduced the electron E_T and P_T spectra as demonstrated in figures 6.6 and 6.7. The separation in R between the electron and the nearest jet, ΔR_{e-jet} , is compared with Monte Carlo in figure 6.8. The two generators displayed different behavior above $\Delta R_{e-jet} \approx 1.2$. Isajet predicted a flat tail, comprising approximately 20% of the distribution. The Single-b generator was in better agreement with the data, which has an integrated number of events in the tail that is consistent with zero. The Isajet distribution was in reasonable agreement with the data in the low ΔR_{e-jet} region; therefore, the region $\Delta R_{e-jet} > 1.2$ was disregarded when making P_T^{sel} distributions.

The charm P_T^{sel} distributions were obtained from ISAJET generated $c\bar{c}$ events. The events were processed in the same manner as the bottom events. Figure 6.9 shows the fits to the P_T^{sel} distributions for electrons from charm.

6.3.4 Fits to Data

The sign subtracted data was fit with the sum of the normalized P_T^{sel} distributions for bottom and charm. The free parameter of the likelihood fit was the fraction of the events due to $b\bar{b}$ production, $f_{b\bar{b}}$. The normalization of the fit was constrained to the observed number of events. The only other parameter was the fraction of the bottom events from indirect b decays, f_{ind} . The value of f_{ind} was determined from branching ratios [16] and the relative acceptance of direct and indirect electrons to be $f_{ind} = 0.09 \pm 0.02$. Each fit was performed twice, the first time fixing f_{ind} at the predicted value and the second time

fixing $f_{ind} = 0$. Figures 6.10 and 6.11 compare the predicted P_T^{rel} distributions for electrons from direct b decays, indirect b decays, and charm decays. The distribution for indirect electrons from b decay is softer than the distribution for the direct. Reducing f_{ind} makes the total bottom distribution less charm-like and the resulting fit tends to overestimate the charm content of the data. By setting f_{ind} to zero, a very conservative assessment of the effect of this parameter upon the fitted value of $f_{b\bar{b}}$ was obtained. The systematic effect of the jet clustering algorithm was investigated by varying the clustering radius and the seed track P_T threshold. The fits are shown in figure 6.12. The results of the fits are summarized in table 6.2. The table lists the fitted values of $f_{b\bar{b}}$ as a function of: the jet clustering radius, $R_{cluster}$; the clustering seed P_T threshold, P_T^{seed} ; the fraction of electrons from indirect b decays relative to direct b decays, f_{ind} ; and the Monte Carlo used to obtain the b P_T^{rel} distributions. The uncertainties listed for $f_{b\bar{b}}$ are from the fit.

R	P_T^{seed} GeV/c	f_{ind}	$f_{b\bar{b}}$ Single- b	$f_{b\bar{b}}$ ISAJET
1.0	1.0	0.09	$1.00^{+0.00}_{-0.01}$	$1.00^{+0.00}_{-0.01}$
1.0	1.0	0.00	$1.00^{+0.05}_{-0.02}$	$1.00^{+0.00}_{-0.01}$
1.0	0.4	0.09	$1.00^{+0.00}_{-0.02}$	$1.00^{+0.00}_{-0.02}$
1.0	0.4	0.00	$1.00^{+0.00}_{-0.04}$	$1.00^{+0.00}_{-0.04}$
0.7	1.0	0.09	$1.00^{+0.00}_{-0.01}$	$1.00^{+0.00}_{-0.01}$
0.7	1.0	0.00	$1.00^{+0.00}_{-0.02}$	$1.00^{+0.00}_{-0.01}$
0.7	0.4	0.09	0.95 ± 0.04	$1.00^{+0.00}_{-0.04}$
0.7	0.4	0.00	0.93 ± 0.04	$0.98^{+0.02}_{-0.04}$
0.4	1.0	0.09	0.87 ± 0.05	$0.93^{+0.04}_{-0.05}$
0.4	1.0	0.00	0.84 ± 0.05	0.90 ± 0.05
0.4	0.4	0.09	0.86 ± 0.05	0.90 ± 0.05
0.4	0.4	0.00	0.83 ± 0.05	0.86 ± 0.05

Table 6.2: A summary of results from fits of $P_T^{rel}(e)$. Single- b and ISAJET refer to the generators used to obtain the P_T^{rel} distributions for electrons from b decay.

$f_{b\bar{b}}$ was found to be 1.0 in the region $R = 1.0 - 0.7$ and decreased by 13% between 0.7 and 0.4, due to decreasing containment of the b -jet. Figure 6.13 shows the Monte Carlo prediction for the fraction of the tracks from the b with $P_T > 0.4$ GeV/c that are clustered as a function of the clustering radius, R . Lowering P_T^{seed} was seen to correspond to at most a 5% change in $f_{b\bar{b}}$. Using $f_{ind} = 0.0$ corresponds to at most a 3% change. Comparison of the results from the two generators estimated the effect of the underlying event and additional activity from the other bottom decay, yielding a 5% effect. The effect of finite statistics upon the subtraction of the fake background was estimated by generating Monte Carlo data sets with the same ratio of fake events to non-fakes observed in the data. The parameterized P_T^{rel} distributions were used to generate sign-subtracted distributions with a $b\bar{b}$ fraction, $f_{b\bar{b}}^{gen}$. The fakes were generated according to the charm distribution to obtain the most conservative result. The distributions were then fit to determine $f_{b\bar{b}}^{fit}$. The probability of obtaining $f_{b\bar{b}}^{fit} = 1.0$ as a function of $f_{b\bar{b}}^{gen}$ is shown in figure 6.14. The 68% confidence level corresponds to a 5% decrease in $f_{b\bar{b}}$.

The P_T^{rel} distributions for the electron and the muon contain the same information concerning $f_{b\bar{b}}$. The value of $f_{b\bar{b}}$ used in this analysis comes only from the electron distribution because of the greater separation power at $E_T > 5$ GeV relative to $P_T(\mu) > 3$ GeV/c. As a check, figure 6.15 shows a fit to the sign-subtracted muon P_T^{rel} distribution with $P_T(\mu) > 3$ GeV/c. The fit yielded a value of 1.00 ± 0.05 for $f_{b\bar{b}}$, where the uncertainty is solely from the fit.

6.3.5 Results

The value of $f_{b\bar{b}}$ was extracted from fitting the sign-subtracted electron P_T^{rel} distribution

Source	Uncertainty (%)
Background subtraction	5
Additional activity	5
Fit	5
P_T^{seed}	5
f_{ind}	3
Total Uncertainty	10

Table 6.3: A summary of the uncertainties associated with $f_{b\bar{b}}$.

with parameterized b and c distributions from Monte Carlo. The value of $f_{b\bar{b}}$ was seen to be independent of the jet clustering radius for values of $R_{cluster}$ between 1.0 and 0.7. Table 6.3.5 lists the estimates of the uncertainties associated with $f_{b\bar{b}}$. The uncertainties were added in quadrature to obtain $f_{b\bar{b}} = 1.00_{-0.10}^{+0.00}$.

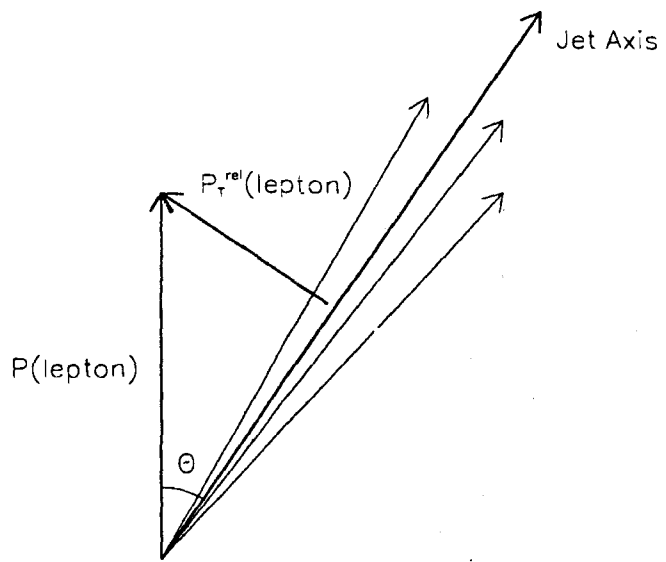


Figure 6.1: An illustration of the definition of P_T^{rel} .

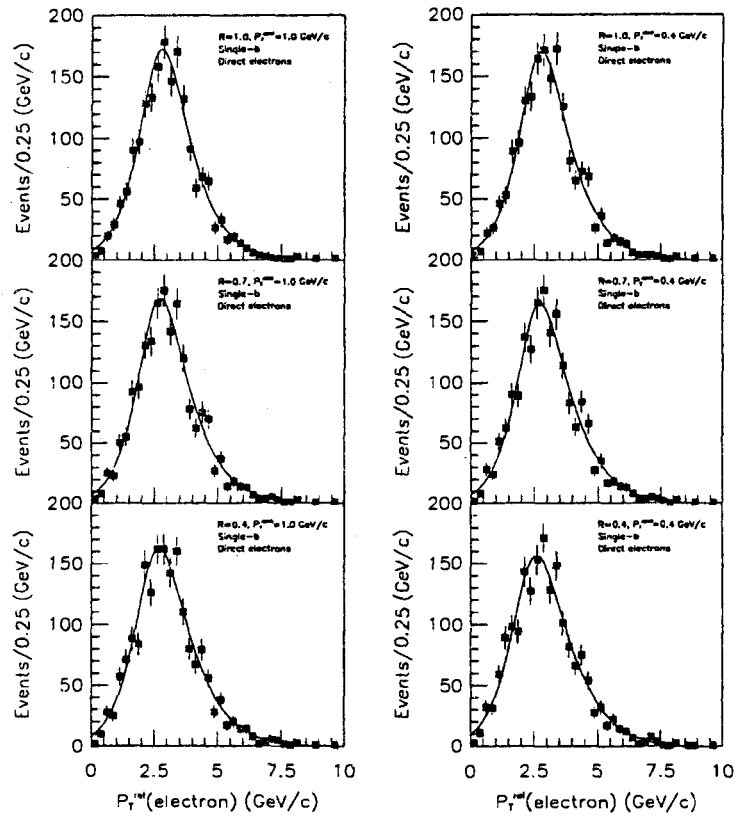


Figure 6.2: Likelihood fits to the direct b electron P_T^{el} distributions from the MNR-based, single- b generator.

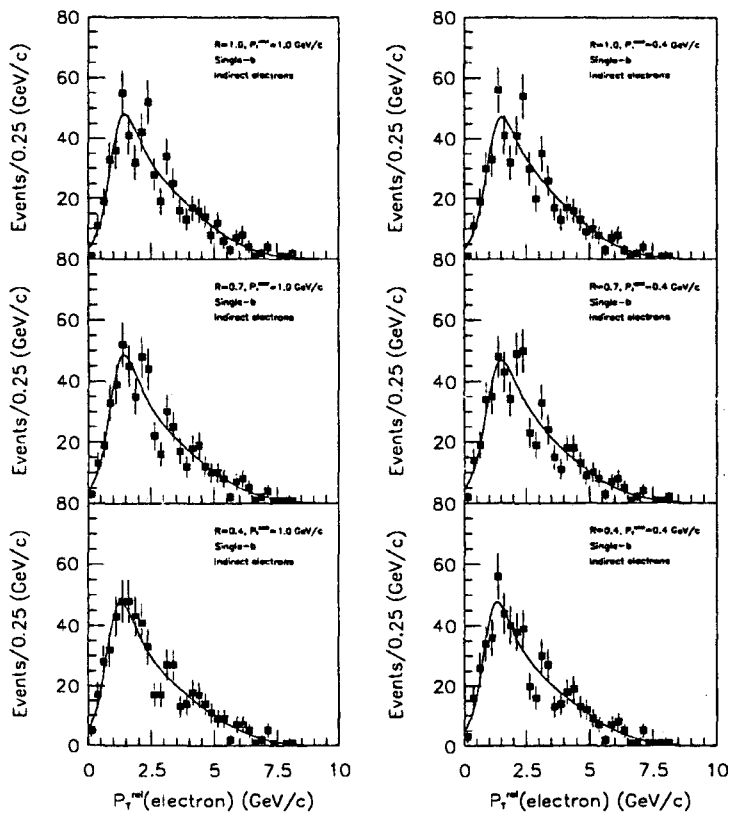


Figure 6.3: Likelihood fits to the indirect b electron P_T^{rel} distributions from the MNR-based, single- b generator.

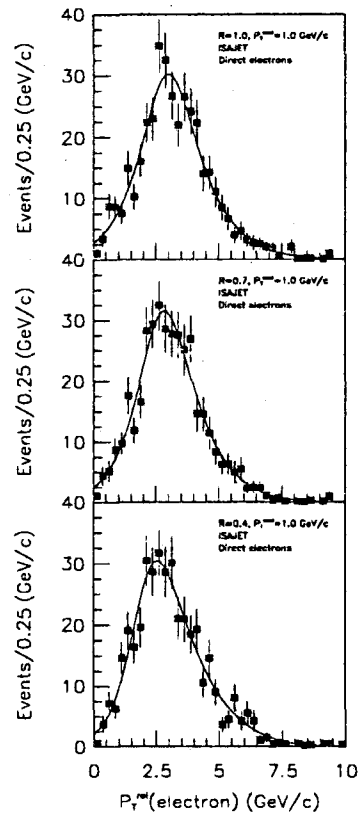


Figure 6.4: Likelihood fits of the direct b electron P_T^{rel} distributions from the Isajet generator.

Figure 6.5: Likelihood fits of the indirect b electron P_7^{rel} distributions from the Isajet generator.

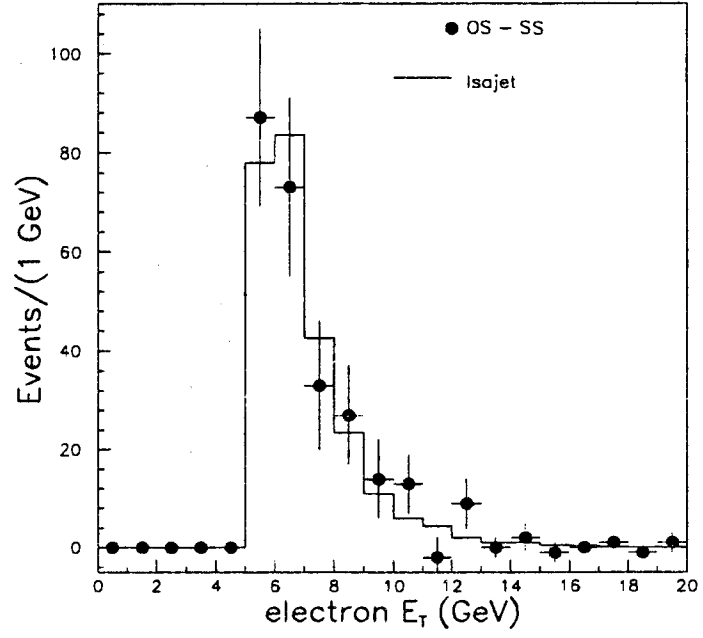


Figure 6.6: A comparison of the sign-subtracted electron E_T distribution from the data with the predictions of the single-b and Isajet generators.

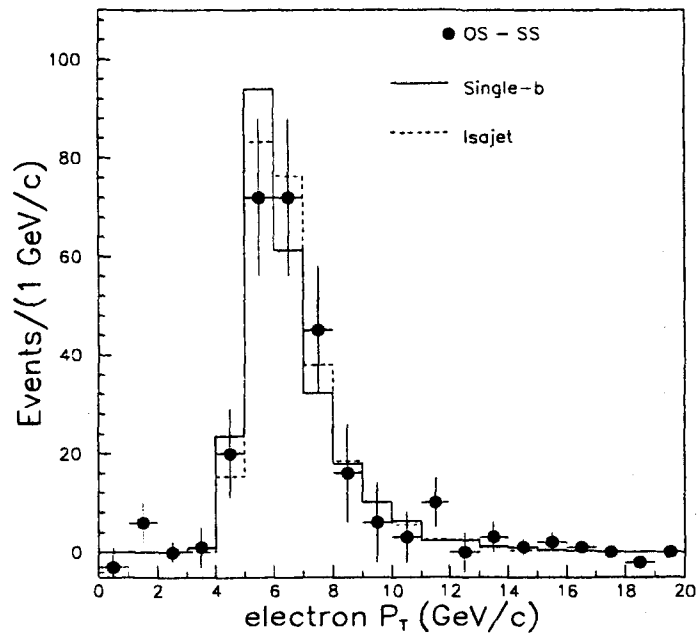


Figure 6.7: A comparison of the sign-subtracted electron P_T distribution from the data with the predictions of the single-b and Isajet generators.

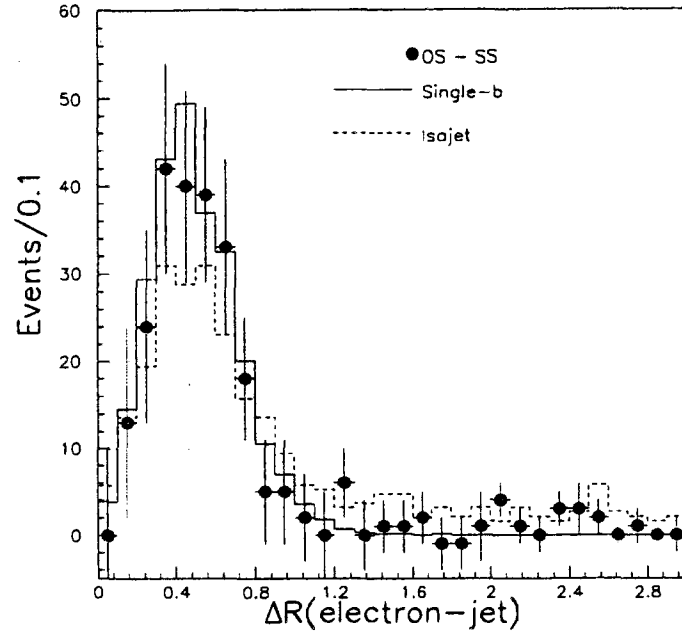


Figure 6.8: Distance in R between the electron and the nearest jet, ΔR .

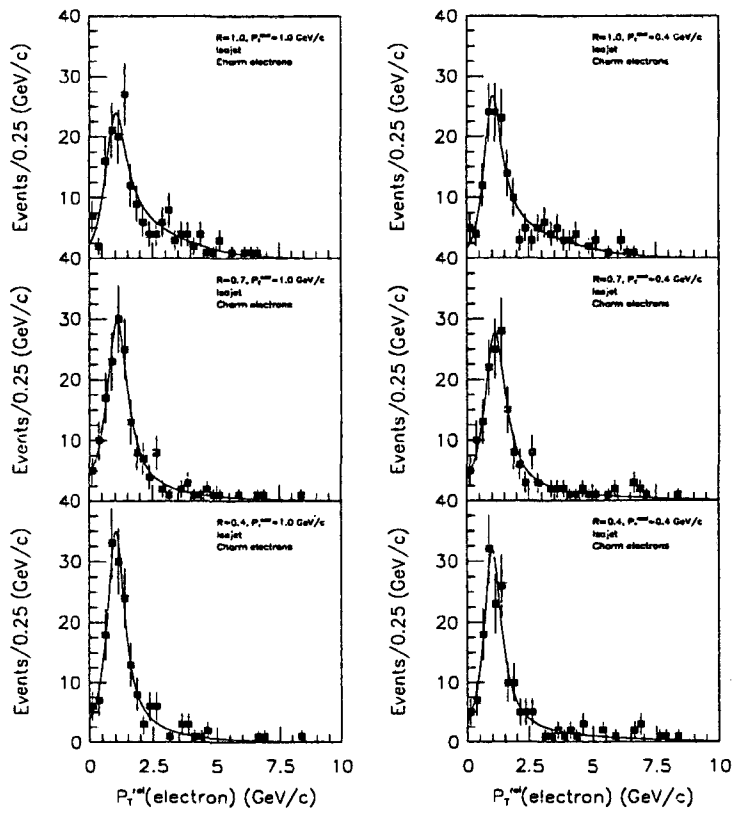


Figure 6.9: Likelihood fits of the charm electron P_T^{rel} distributions.

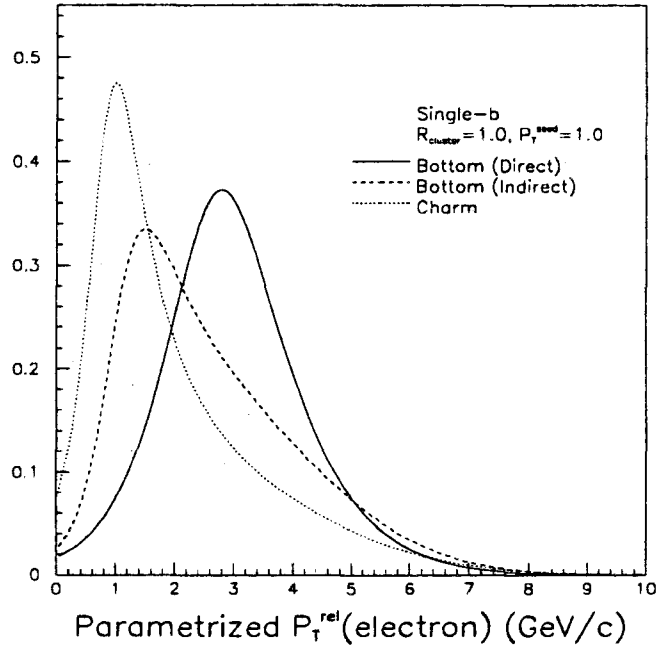


Figure 6.10: Comparison of the single-b electron P_T^{rel} parameterizations for direct b, indirect b, and charm.

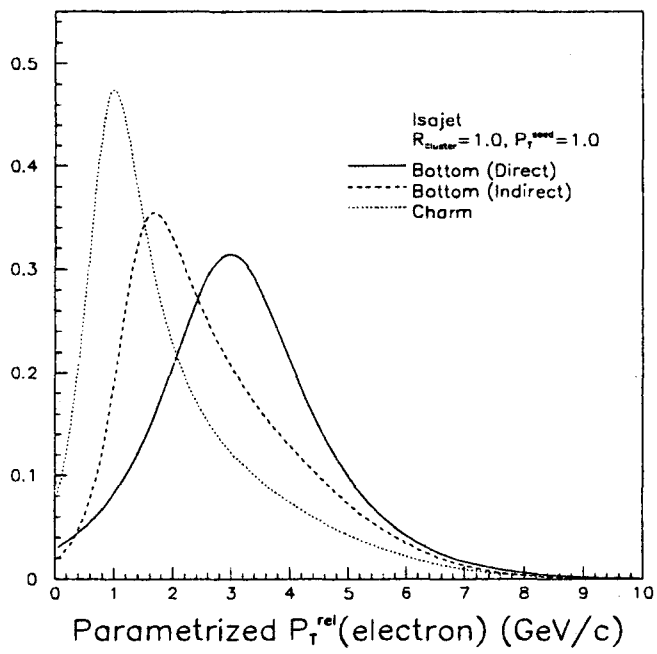


Figure 6.11: Comparison of the Isajet electron P_T^{rel} parameterizations for direct b , indirect b , and charm.

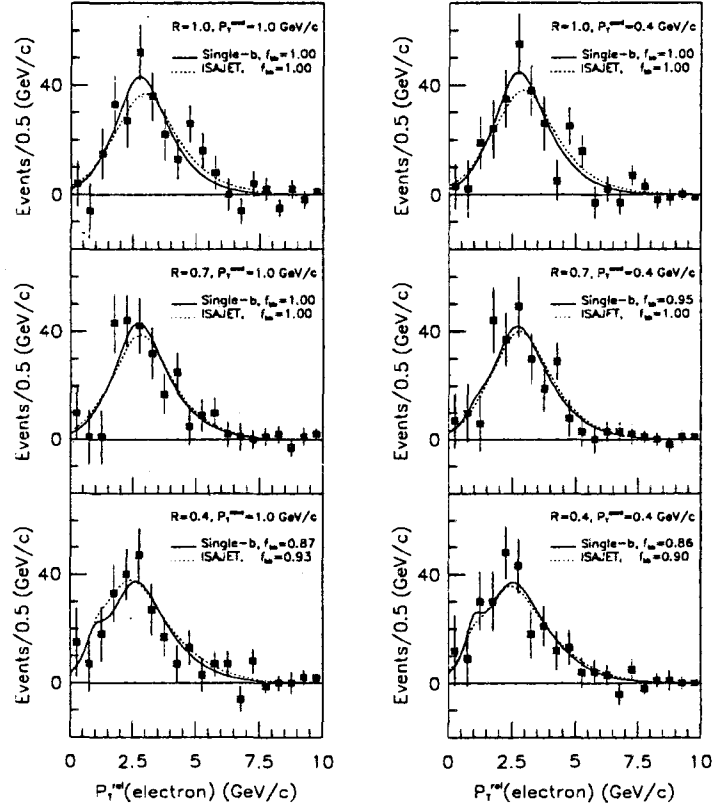


Figure 6.12: Likelihood fits of the normalized b and c P_T^{cd} parameterizations to the sign-subtracted electron P_T^{cd} distribution from the data. The free parameter of the fit is $f_{b\bar{b}}$, the fraction of the data due to $b\bar{b}$ production. Fits are shown for three values of the clustering radius, R , and for two choices of clustering seed track P_T threshold, P_T^{seed} .

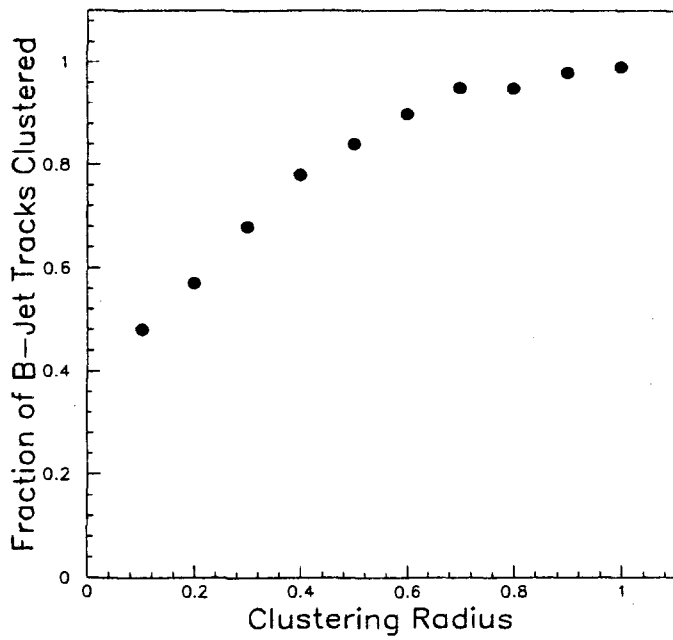


Figure 6.13: The fraction of the tracks, with $P_T > 0.4$ GeV/c, from the b -jet that get clustered as a function of the clustering radius, R .

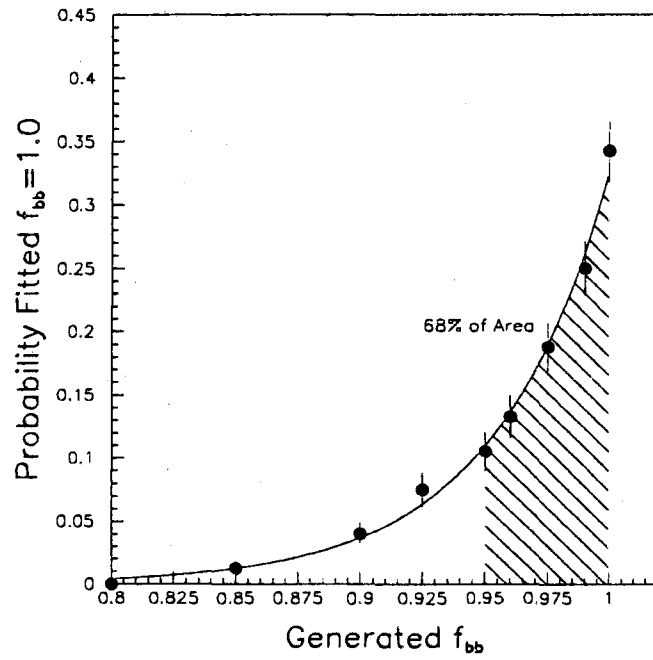


Figure 6.14: The probability of obtaining a fitted value of $f_{bb} = 1.0$ (f_{bb}^{fit}) as a function of the real f_{bb} (f_{bb}^{gen}).

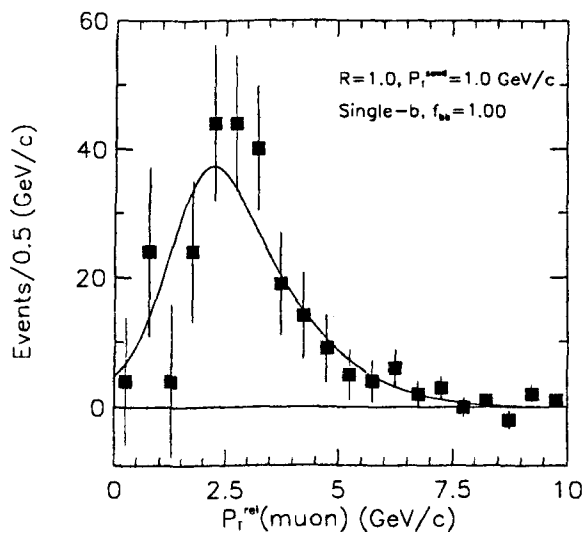


Figure 6.15: A likelihood fit of the sum of the normalized b and c $P_T^{rel}(\mu)$ distributions to the sign-subtracted $P_T^{rel}(\mu)$ distribution from the data.

6.4 Cuts Efficiency ϵ_{cuts}

ϵ_{cuts} was defined as the ratio of the opposite sign excess due to $b\bar{b}$ production after and before the imposition of the event selection cuts; as such, it is essentially the efficiency of the cuts for $e\mu$ pairs from $b\bar{b}$ production.

$$(6.22) \quad \epsilon_{cuts} \equiv \frac{\Delta_{b\bar{b}}^{(2)}}{\Delta_{b\bar{b}}^{(1)}} = \frac{f_{b\bar{b}}^{(2)} \Delta_{e\mu}^{(2)}}{f_{b\bar{b}}^{(1)} \Delta_{e\mu}^{(1)}}.$$

For calculational purposes, the total efficiency, ϵ_{cuts} , was separated into two components:

$\epsilon_{cuts} = \epsilon_1 \epsilon_2$, where ϵ_1 referred to the cuts involving the matching of a muon track with either the event vertex or hits in the muon chambers and ϵ_2 referred to all remaining cuts.

ϵ_1 was determined from a sample of $J/\psi \rightarrow \mu^+ \mu^-$ events where both muons had $P_T > 3.0$ GeV/c. The dimuon invariant mass distribution is shown in figure 6.16. The invariant mass distribution was fitted with a combination of a gaussian and a first order polynomial. The number of actual J/ψ events falling within three sigma of the peak was determined by subtracting the integrated linear background from the total number of events in the region. This procedure was repeated after application of the muon track matching cuts. In this manner, the number of muons tested and the number passing were determined. Table 6.4 summarizes the efficiencies of the individual cuts and the total efficiency, ϵ_1 . The uncertainty associated with ϵ_1 was obtained by adding the individual uncertainties in quadrature. Figures 6.17 through 6.20 show the distributions of the quantities used for muon selection. The distributions are background subtracted.

ϵ_2 was determined from the unbiased data set. As discussed in section 6.3, the analysis data set yielded a value of $1.0_{-0.1}^{+0.0}$ for $f_{b\bar{b}}^{(2)}$. An attempt was made to determine $f_{b\bar{b}}^{(1)}$ in

Cut	Efficiency
Track-Stub match in $x < 3\sigma$	0.998 ± 0.001
Track-Stub match in $z < 3\sigma$	0.998 ± 0.001
$ z_{track} - z_{vertex} < 5 \text{ cm.}$	0.97 ± 0.01
Track DCA $< 50 \text{ mm.}$	$1.000^{+0.000}_{-0.002}$
ϵ_1	0.97 ± 0.01

Table 6.4: ϵ_1 and component efficiencies.

the same manner by fitting the electron P_T^{rel} distribution from the unbiased data set with the appropriate Monte Carlo derived distributions. The fit to the electron P_T^{rel} distribution from the unbiased data set is shown in figure 6.21 for $P_T(\mu) > 3 \text{ GeV}/c$. The poor quality of the fit was due to the dual problems of the unbiased data set: low statistics and a large background from fakes. For comparison, figure 6.22 show the fit to the same distribution after the imposition of all cuts. Due to the unconvincing nature of the fit, another method was used to estimate ϵ_2 . Defining: $R \equiv \frac{\Delta_{\mu}^{(2)}}{\Delta_{\mu}^{(1)}}$ and $\epsilon_{c\bar{c}} \equiv \frac{N_{c\bar{c}}^{(2)}}{N_{c\bar{c}}^{(1)}}$, equation 6.22 may be recast as

$$(6.23) \quad \epsilon_{cuts} = R \left[\frac{1}{f_{b\bar{b}}^{(2)}} - \frac{R}{\epsilon_{c\bar{c}}} \left(\frac{1}{f_{b\bar{b}}^{(2)}} - 1 \right) \right]^{-1}.$$

$\epsilon_{c\bar{c}}$ was estimated from the data by finding the efficiency of the cuts for $e\mu$ events with $P_T^{rel}(e) < 2 \text{ GeV}/c$. This interval was motivated from examination of figure 6.10 and represents the range in which the $c\bar{c}$ probability is maximal relative to the $b\bar{b}$ probability. Table 6.5 shows R , $\epsilon_{c\bar{c}}$, ϵ_1 , ϵ_2 , and ϵ_{cuts} as a function of the muon P_T threshold. The accuracy of the estimate for $\epsilon_{c\bar{c}}$ proved to be unimportant as $f_{b\bar{b}}^{(2)} = 1.0$, meaning that $\epsilon_{c\bar{c}}$ entered only into the calculation of the uncertainty associated with ϵ_2 . The distributions of the electron and muon selection quantities are shown for the unbiased $e\mu$ data set in figures 6.23 through 6.24. The figures show the opposite sign, same sign, and sign-subtracted

distributions.

$P_T(\mu) > \text{GeV}/c$	3.0	4.0	5.0
R	0.71 ± 0.27	0.54 ± 0.21	0.42 ± 0.21
$\epsilon_{c\bar{c}}$	0.38 ± 0.49	0.43 ± 0.60	0.24 ± 0.30
ϵ_2	0.71 ± 0.27	0.54 ± 0.21	0.42 ± 0.21
ϵ_1	0.97 ± 0.01	0.97 ± 0.01	0.97 ± 0.01
ϵ_{cuts}	0.69 ± 0.27	0.52 ± 0.21	0.41 ± 0.21

Table 6.5: ϵ_{cuts} and associated values as a function of $P_T(\mu)$. $\epsilon_{cuts} = \epsilon_1 \epsilon_2$.

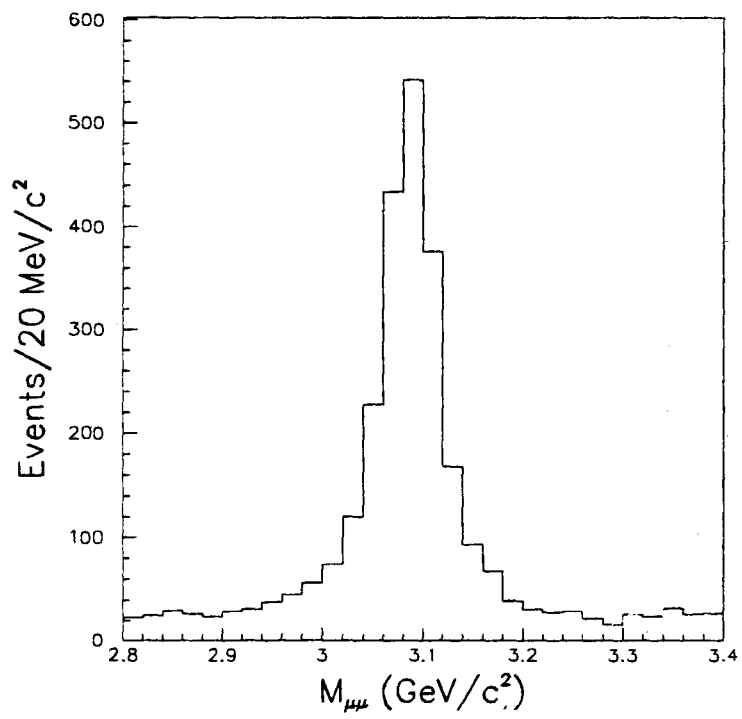


Figure 6.16: Dimuon invariant mass in the J/ψ mass region.

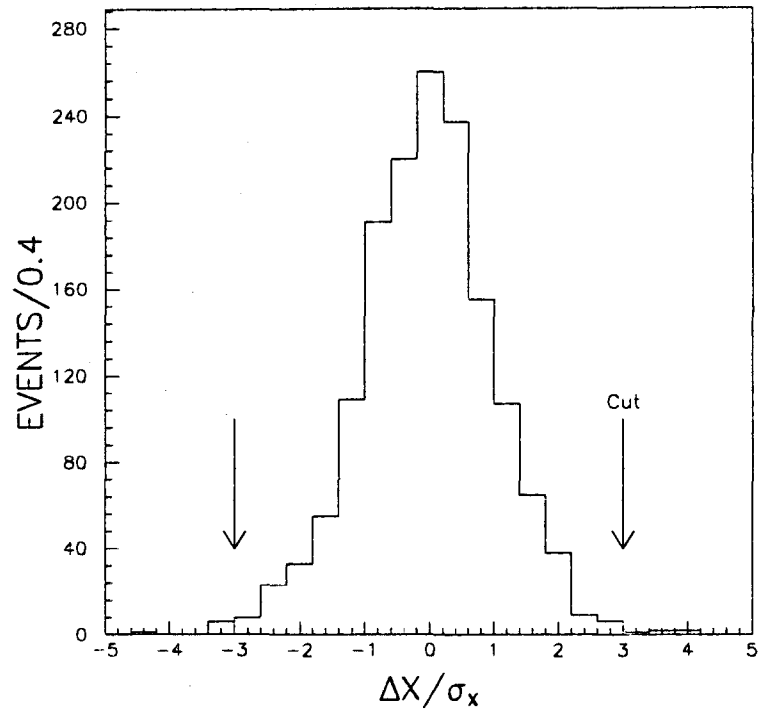


Figure 6.17: The distribution of track-stub intercept matching in the zy plane for dimuon events within one σ of the J/ψ mass.

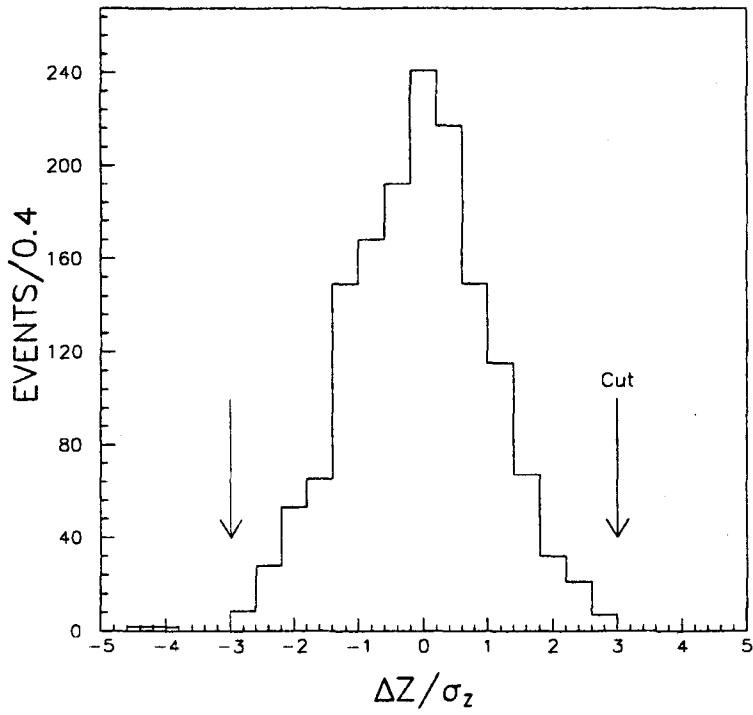


Figure 6.18: The distribution of track-stub intercept matching in the zy plane for dimuon events within one σ of the J/ψ mass.

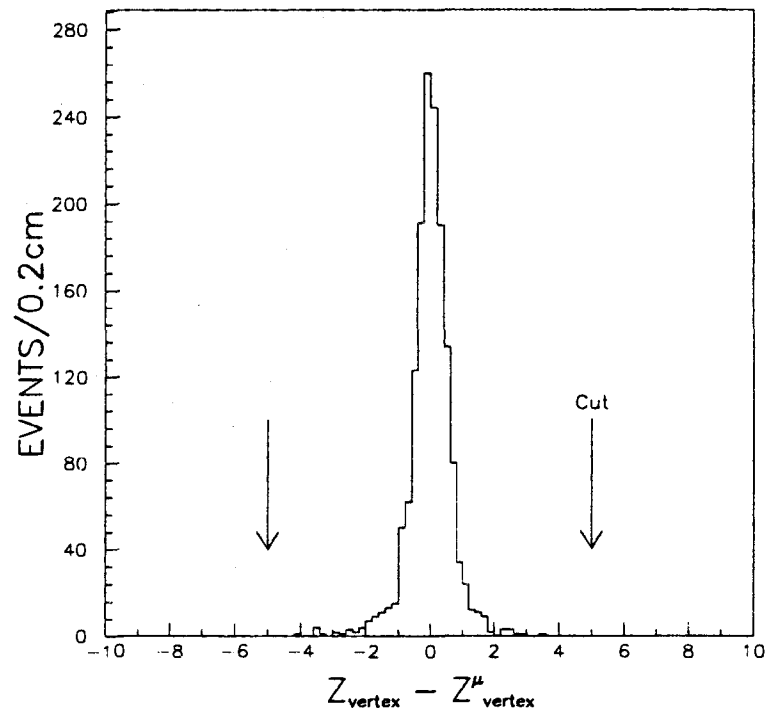


Figure 6.19: The distance in z of the μ track from the z vertex at the distance of closest approach. The distribution is for dimuon events within one σ of the J/ψ mass

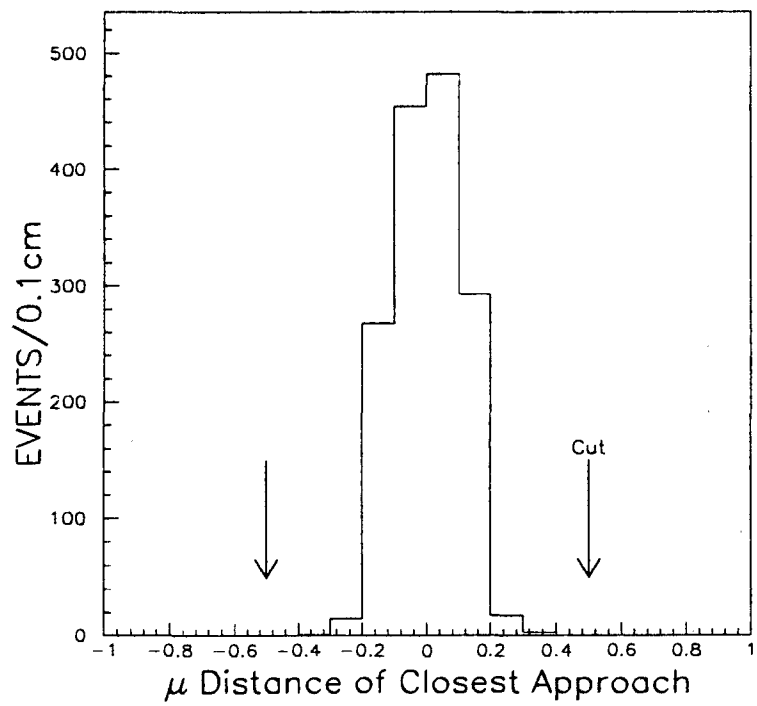


Figure 6.20: The muon track distance of closest approach. The distribution is for dimuon events within one σ of the J/ψ mass.

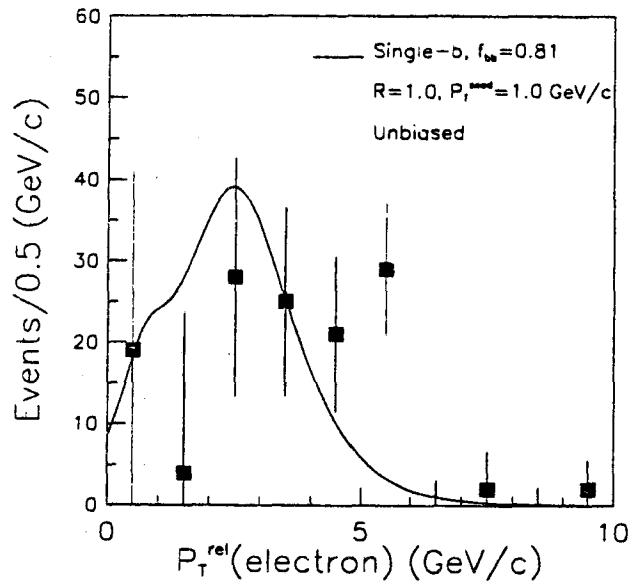


Figure 6.21: A likelihood fit of the sum of the normalized b and c electron P_T^{rel} distributions to the sign-subtracted electron P_T^{rel} distribution from the unbiased data set. The data set was not subjected to the electron selection cuts.

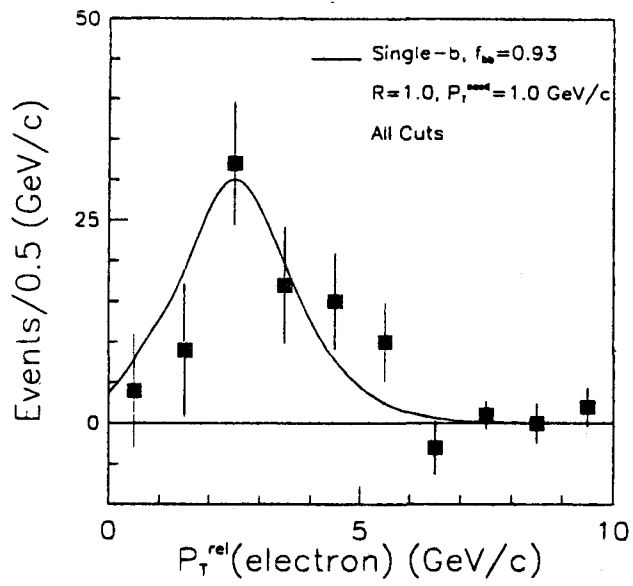


Figure 6.22: A likelihood fit of the sum of the normalized b and c electron P_T^{rel} distributions to the sign-subtracted electron P_T^{rel} distribution from the unbiased data set. The data was subjected to all electron selection cuts.

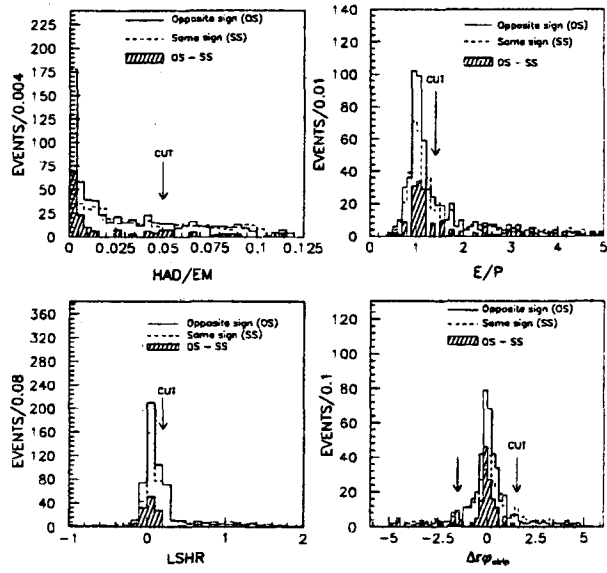


Figure 6.23: Distributions of electron quality variables for the unbiased $e\mu$ sample.

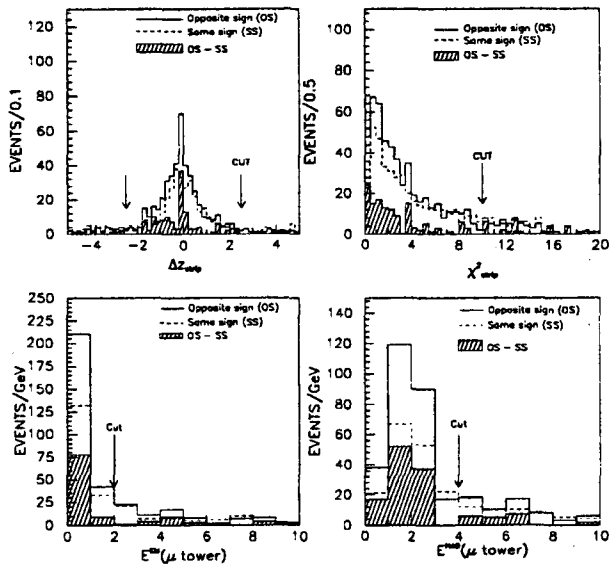


Figure 6.24: Distributions of electron and muon quality variables for the unbiased $e\mu$ sample.

6.5 Acceptances

The acceptance for electrons and muons from bottom quark decays was determined from Monte Carlo. Bottom quarks were generated with the P_T spectra obtained from the full NLO calculation of $b\bar{b}$ production by Mangano, Nason, and Ridolfi (MNR). Peterson fragmentation was used to produce hadrons from the quarks. The hadrons were then decayed semileptonically according to the model of Isgur, Scora, Grinstein, and Wise (ISGW). The MNR calculation is described in chapter 2. The Peterson fragmentation model and the ISGW model are discussed in the following subsections. The final subsection describes the acceptance calculation and presents the results.

6.5.1 Peterson Fragmentation

Fragmentation falls outside the boundaries of what is calculable with perturbative QCD. Thus models have been introduced in the attempt to obtain a description of these processes. A model that is often used to describe heavy quark fragmentation is that due to Peterson *et al.* [18].

The Peterson model provides an expression for the heavy quark fragmentation function, $D(z)$, as a function of only one parameter, ϵ_p :

$$D(z) = \frac{N(1-z)^2}{[(1-z)^2 + \epsilon_p z]^2}.$$

z is the fraction of the energy plus momentum of the initial quark that is carried by the final hadron

$$z = \frac{(E + P_{||})_H}{(E + P)_Q},$$

where P_{\parallel} is the component of the hadron momentum parallel to the direction of the initial heavy quark. N is a normalization constant. Properly normalized, $D(z)$ yields the probability of obtaining a particular value of z . ϵ_p is an experimentally determined parameter. Present measurements imply $\epsilon_p = 0.006 \pm 0.002$ [17] for bottom quarks. The ϵ_p dependence of $D(z)$ is illustrated in figure 6.29.

The momentum of the hadron transverse to the direction of the initial heavy quark, P_{\perp} , is not specified by $D(z)$. The mean value of P_{\perp} was estimated from uncertainty principle arguments to be approximately 350 MeV/c. P_{\perp} was assumed to be distributed according to the functional form $(1 + \alpha P_{\perp}^2)$, where α was chosen so as to yield 350 MeV/c as the mean value of P_{\perp} .

6.5.2 The ISGW Model

The model of semileptonic B and D meson decays due to Isgur, Scora, Grinstein, and Wise is detailed in the literature [15]. In contrast to the spectator model, which treats the heavy quark component of a meson as a free particle, the ISGW model treats the heavy quark-light quark bound state. Due to the mass of the heavy quark, the problem is treated in a non-relativistic manner. The Schrödinger equation is solved for a Coulomb plus linear potential with a variational method utilizing the basis states of the three-dimensional harmonic oscillator.

6.5.3 The Acceptance

Semileptonic decays do not allow the reconstruction of the quark P_T ; hence, this analysis used lepton acceptances expressed in terms of a quark P_T threshold, P_T^{\min} . The acceptance

for a lepton, ℓ , from a bottom decay was defined as follows:

$$A(b\ell) = \frac{\text{Number of } b\text{'s decaying to fiducial } \ell\text{'s with } P_T(\ell) > P_T^{\text{thresh}}(\ell) \text{ and } |z_{\text{vertex}}| < 60\text{cm}}{\text{Number of } b\text{'s decaying to } \ell\text{'s with } |y_b| < 1 \text{ and } P_T(b) > P_T^{\text{min}}}$$

The fiducial region of the detector referred to the portions of the detector efficient for the detection of the lepton in question. The choice of a value for P_T^{min} was essentially arbitrary. In this analysis, the convention of [1] was followed and P_T^{min} was chosen such that 90% of the bottom decays with $P_T(\ell) > P_T^{\text{thresh}}$ have $P_T(b) > P_T^{\text{min}}$. The shape of the accepted b quark P_T distribution, and thus the value of P_T^{min} , is dependent upon $P_T^{\text{thr}}(\ell)$, the lepton P_T threshold.

The combined acceptance of the electron-muon pair was assumed to factorize into the product of the acceptance for the electron only and the acceptance for the muon only. The P_T distribution for b quarks with $|y_b| < 1$ that decay semileptonically to an electron is shown in figure 6.28. The upper distribution is for all electrons. The lower distribution is for electrons with $P_T > 5$ GeV/c. The equivalent distributions for b quarks that produce muons are shown in figures 6.25, 6.26, and 6.27 for muon P_T thresholds of 3, 4, and 5 GeV/c. The values of P_T^{min} extracted from the figures are shown in table 6.6.

$P_T^{\text{thr}}(\ell)$ GeV/c	P_T^{min} GeV/c
3.0	6.50
4.0	7.50
5.0	8.75

Table 6.6: P_T^{min} of a b quark that decays semileptonically as a function of the lepton P_T threshold, $P_T^{\text{thr}}(\ell)$.

The justification for factorizing the acceptance came from an investigation of the NLO calculation of $b\bar{b}$ production. Figure 6.30 shows the P_T^{min} of the second b in the event, P_T^{min2} , as a function of the P_T^{min} of the first, P_T^{min1} . A P_T cut of 5 GeV/c on the lepton originating from the first b would yield a value of about 9 GeV/c for P_T^{min1} . Consulting the figure, it is seen that the corresponding theoretical expectation for P_T^{min2} is about 3.5 GeV/c. If the second b is required to produce a lepton with $P_T > 3$ GeV/c, however, the expected P_T^{min} is 6.5 GeV/c. This indicates that the observed portion of the P_T spectrum for the second b is well above any bias introduced by the P_T threshold on the first b .

The results of the acceptance calculation are listed in table 6.7. The acceptance for directly produced leptons ($b \rightarrow c\ell\nu$) is represented by $A(b\ell)$. $\alpha(\ell)$ denotes the ratio of the acceptance for indirectly produced leptons ($b \rightarrow cX, c \rightarrow s\ell\nu$) relative to the acceptance for directly produced leptons. The systematic uncertainties resulted from the variation of the fragmentation parameter and the shape of the b P_T spectra. The fragmentation parameter was varied in the range: $0.004 < \epsilon_p < 0.008$, which corresponded to a 10% variation in the acceptance. The shapes of the b P_T spectra were varied and resulted in a 15% variation in acceptance.

$P_T^{thr}(\ell)$	$P_T(e) > 5$ GeV/c	$P_T(\mu) > 5$ GeV/c	$P_T(\mu) > 4$ GeV/c	$P_T(\mu) > 3$ GeV/c
$A(b\ell)$	0.153 ± 0.028	0.092 ± 0.017	0.099 ± 0.018	0.116 ± 0.021
$\alpha(\ell)$	0.099 ± 0.005	0.126 ± 0.011	0.130 ± 0.008	0.182 ± 0.006

Table 6.7: The acceptances of electrons and muons from b decays. $A(b\ell)$ denotes the acceptance of leptons from direct decays ($b \rightarrow c\ell\nu$), and $\alpha(\ell)$ represents the ratio of the acceptance for leptons from indirect decays ($b \rightarrow cX, c \rightarrow s\ell\nu$) relative to the acceptance for direct decays.

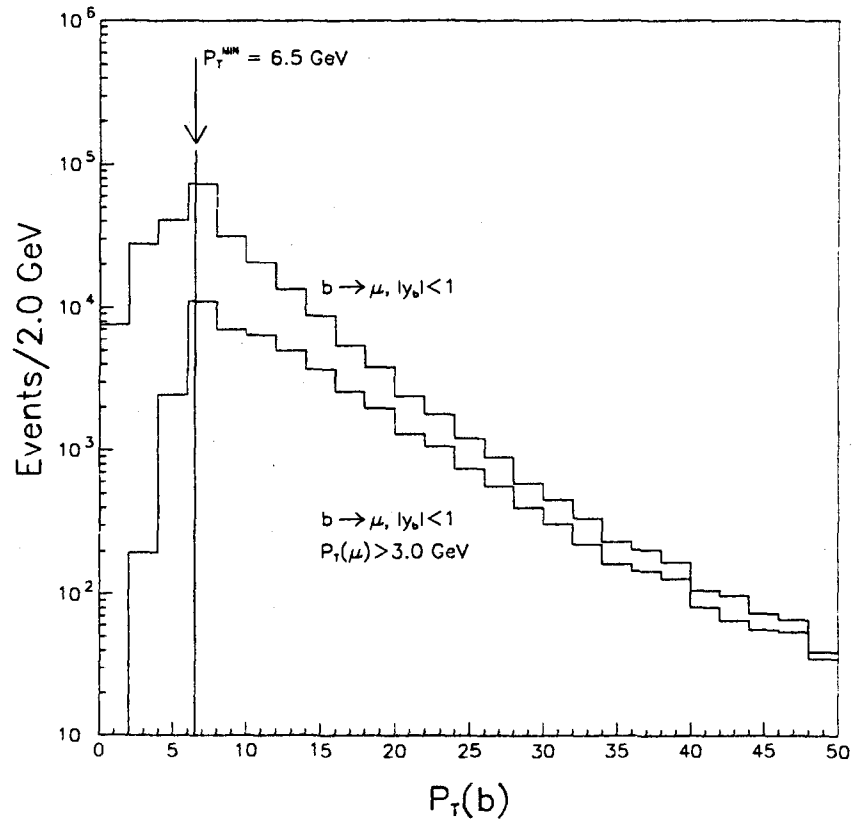


Figure 6.25: P_T for all bs generated with $|y_b| < 1$ and that produce a μ (*upper*) and the subset of those for which $P_T(\mu) > 3.0 \text{ GeV}$. (*lower*).

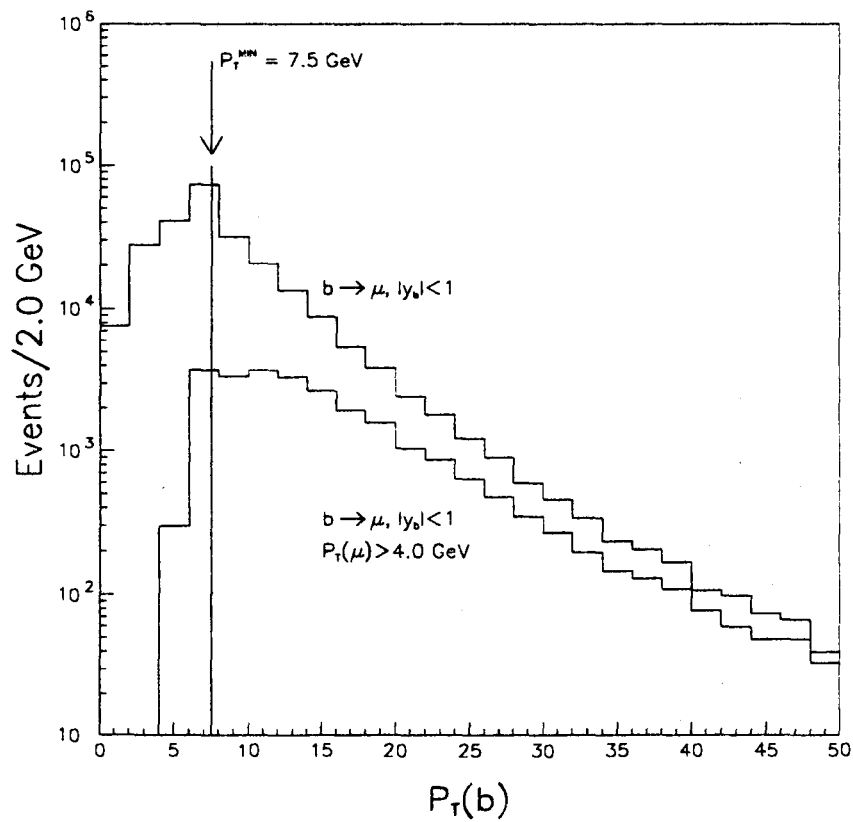


Figure 6.26: P_T for all bs generated with $|y_b| < 1$ and that produce a μ (*upper*) and the subset of those for which $P_T(\mu) > 4.0$ GeV. (*lower*).

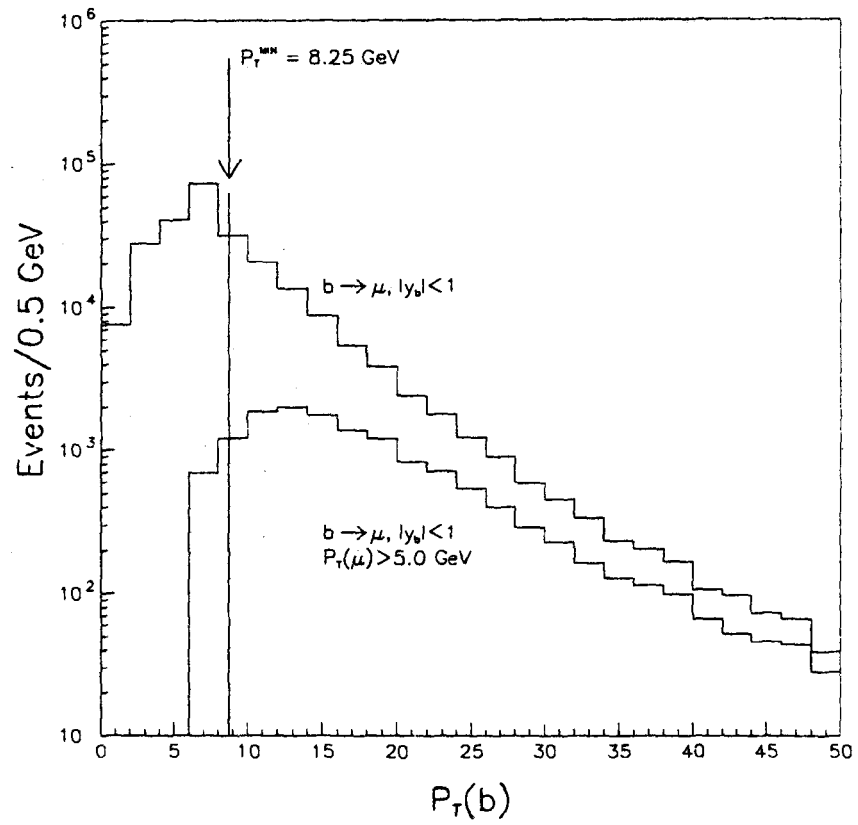


Figure 6.27: P_T for all b s generated with $|y_b| < 1$ and that produce a μ (*upper*) and the subset of those for which $P_T(\mu) > 5.0$ GeV (*lower*).

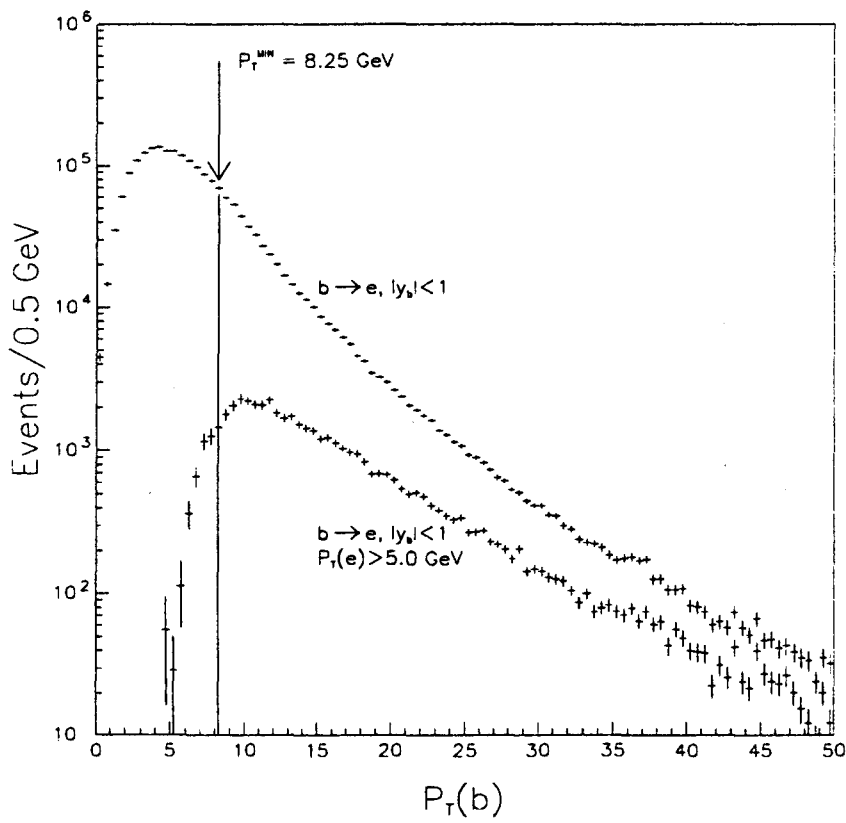


Figure 6.28: P_T for all b s generated with $|y_b| < 1$ and that produce an electron (*upper*) and the subset of those for which $P_T(e) > 5.0$ GeV. (*lower*).

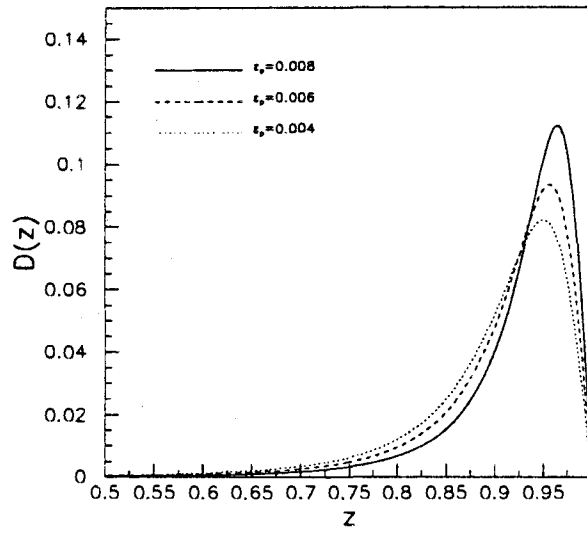


Figure 6.29: The variation of the Peterson fragmentation function, $D(z)$, with the fragmentation parameter, ϵ_p .

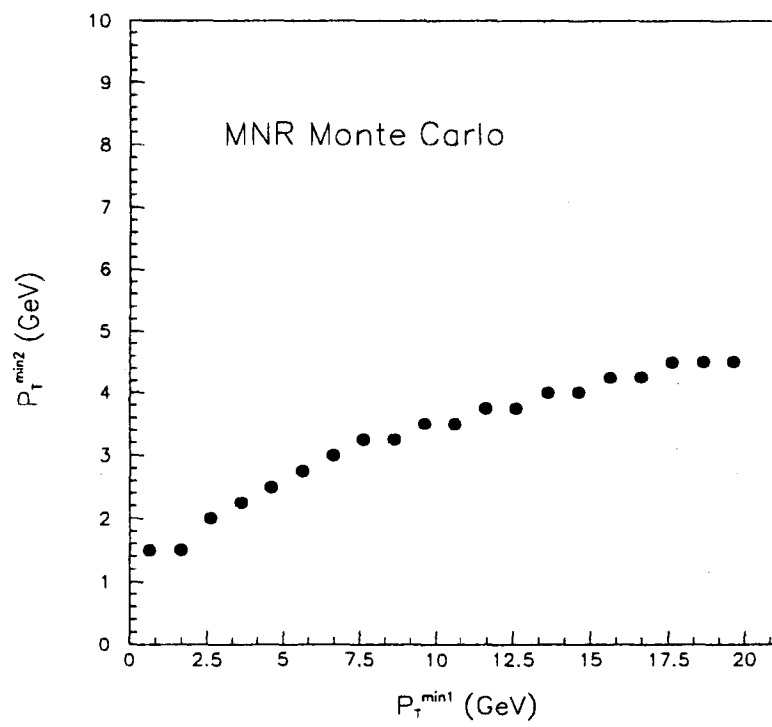


Figure 6.30: The MNR prediction for the variation of P_T^{min2} with P_T^{min1} .

6.6 Trigger Efficiency

As was discussed in chapter 3, the rate of $p\bar{p}$ collisions at the Tevatron was too large to allow information about every event to be collected, necessitating the use of a triggering system to identify events of particular interest. For each event tested, the trigger compared detector information with preset criteria to determine whether the event should be accepted. There were many sets of criteria, or 'triggers', each motivated by interest in events of a particular type.

The data used in this analysis were collected by the ELECTRON EMC.5.CMU.3 trigger. This trigger required a central electron with $E_T > 5$ GeV and a central muon with $P_T > 3$ GeV/c. The detailed requirements of this trigger are presented in the following subsection. The remaining subsections describe how the efficiencies of the trigger requirements were determined, and how the individual efficiencies were combined to obtain the total trigger efficiency.

6.6.1 The Trigger Requirements

Muon Requirements

Muon triggers were based upon reconstructed tracks, or 'stubs', in the muon chambers, and tracks found in the CTC by the Central Fast Tracker (CFT). In both cases, the track reconstruction took place in the $r - \phi$ plane, utilizing no z information.

The Level 1 muon trigger requirement was the presence of a stub with $P_T > 3$ GeV. The P_T of the muon was calculated in Level 1 from the angle of incidence, α , that the stub made relative to a radial line. Figure 6.31 shows the geometrical quantities involved in the

calculation.

As a muon travels through the solenoidal magnetic field, $B = 1.4116$ T, it follows a curved path with a chord L , where $L = 1.44$ m is the radius of the solenoid field. Outside of the magnetic field, the muon follows a straight path to intersect the muon chambers at an angle, α , relative to the radial direction. The angle of deflection, β , is related to the P_T via

$$\sin \frac{\beta}{2} = \frac{eLB}{2P_T},$$

where e is the electric charge of the muon in units of the electron charge. Using

$$L \sin \frac{\beta}{2} = D \sin \alpha,$$

where $D = 3.470$ m is the distance from the origin to the muon chambers,

$$\sin \alpha = \frac{eL^2B}{2DP_T}.$$

In the small angle approximation, this becomes

$$\alpha \approx \frac{eL^2B}{2DP_T}.$$

Level 2 first required a match in $r - \phi$ between a muon stub passing Level 1 and a CFT track. Each CFT track was propagated through the solenoid and the calorimetry to the radius of the muon chambers. The propagation included the effects of the magnetic field in the solenoid. The track was considered to match the stub if it propagated to either the

muon chamber containing the stub or an adjacent chamber. Thus, the maximum possible angular distance in the transverse plane between the track and the stub was 10.8° . After finding a matching CFT track, Level 2 further required that the track pass a $3 \text{ GeV}/c$ P_T threshold.

Electron Requirements

Electron triggers were based upon information from the central calorimeters and the CFT. The trigger did not use the full granularity of the calorimeters. Instead 'trigger towers' were used, which were twice the size of the calorimeter towers. Two adjacent calorimeter towers in η were ganged together to form one trigger tower of $\delta\eta \times \delta\phi = 0.2 \times 15^\circ$ in size. The trigger tower energies were weighted by $\sin\theta$ to represent the transverse energy.

Level 1 operated by requiring at least one trigger tower have weighted energy above 3 GeV. In Level 2, CEM trigger clusters were formed by initially looking for 'seed' towers with $E_T > 3 \text{ GeV}$. Adjacent towers were added to the cluster if they passed an E_T threshold of 1 GeV. The total $EM E_T$ is obtained from a scalar sum of the transverse energies of the towers comprising the cluster. The total E_T ($EM + HAD$) of the cluster is obtained in the same fashion. Level 2 required that the total E_T of the cluster be greater than or equal to 5 GeV, and that the ratio of the total E_T to the $EM E_T$ be less than 1.125. The final Level 2 requirement was a CFT track with $P_T > 4.8 \text{ GeV}/c$ that matched the cluster in $r - \phi$.

Efficiency of Muon Requirements

The efficiency of both the Level 1 and Level 2 muon trigger requirements were determined in a separate analysis [12]. A brief description of the method is given below.

The determination of the efficiency of the Level 1 muon trigger requirements began with the selection of a sample of unbiased muon candidates. Such a sample was obtained by selecting muon candidates from events passing triggers independent of the central muon system. The muon candidates were stubs in the central muon chambers which had been associated with tracks in the CTC. Candidate muons can be real muons, non-prompt muons from pion or kaon decays, interacting punch-through, or non-interacting punch-through. Non-interacting punch-through refers to charged pions or kaons that traverse the calorimetry without interacting. For the purpose of studying the trigger, non-interacting punch-through is indistinguishable from real muons and should cause no bias. Interacting punch-through, such as particles from a jet that leak out the back of the calorimeter or from late showering particles, will be a source of bias as the P_T of the resultant muon stub and the P_T of the CTC track are related through other physics than just the effect of the trigger system. The fraction of the muon candidates due to interacting punch-through was determined from the examination of the energy deposition in the hadronic calorimeter tower traversed by the candidate. Real muons and non-interacting punch-through will produce a distribution consistent with a minimum ionizing particle (MIP), *i.e.*, a Vavilov² distribution. Interacting punch-through was seen to produce a flat distribution. The muon candidates were binned in P_T and the hadronic energy distribution within each bin fit with a Vavilov distribution plus a flat background. The muon candidates were then subjected to the Level 1 requirements and the resulting distribution refit. The ratio of the number of remaining, Vavilov-distributed events to the initial number was taken as the efficiency of the Level 1 requirements for muons. The resulting Level 1 efficiency, as a function of reconstructed muon P_T , is shown

²The Vavilov distribution reduces to the Landau distribution for the special case of thin absorbers.

in figure 6.32.

The efficiency of the Level 2 trigger requirement was also determined from the muon candidates. Candidates passing the Level 1 requirements were tested for a matching CTC track with $P_T > 3 \text{ GeV}/c$. The efficiency of the Level 2 requirements are shown in figure 6.33 as a function of the reconstructed muon P_T .

Efficiency of Electron Requirements

The efficiency of the 5 GeV cluster E_T threshold in Level 2 was driven by differences between the values of E_T used in Level 2, E_T^{L2} , and those reconstructed in the analysis, E_T^{ana} . E_T^{L2} was calculated by the trigger hardware and was intended to be a rapidly obtainable approximation to the “true” electron transverse energy. E_T^{ana} was reconstructed with software and provided a better measure of the electron E_T than E_T^{L2} by utilizing more detector information and by applying detector calibrations and energy corrections.

The relationship between E_T^{L2} and E_T^{ana} was investigated using a sample of electrons unbiased by trigger requirements; such a sample was obtained by selecting electrons from events which satisfied an inclusive muon trigger. The Level 2 response, E_T^{L2}/E_T^{ana} , was parameterized by a gaussian, both before and after the imposition of the 5 GeV E_T^{L2} threshold. The fitted means (μ) and the fitted standard deviations (σ) are shown in figure 6.34 as a function of the E_T^{ana} interval. The values of μ and σ are listed in table 6.8. The E_T^{L2} threshold was seen to have little effect on the μ and σ values for $E_T^{ana} > 8 \text{ GeV}$.

Given that E_T^{L2}/E_T^{ana} is gaussian distributed, the efficiency of a 5 GeV E_T^{L2} threshold is readily calculable. Defining s as the number of standard deviations from the mean that an electron with reconstructed transverse energy E_T^{ana} need fluctuate in order to pass a 5

E_T Range (GeV)	Volunteers $E_T^{L2} > 0$ GeV		Volunteers $E_T^{L2} > 5$ GeV	
	Fitted μ	Fitted σ	Fitted μ	Fitted σ
5 - 6	0.83 ± 0.01	0.11 ± 0.01	0.92 ± 0.01	0.06 ± 0.01
6 - 7	0.82 ± 0.01	0.13 ± 0.01	0.88 ± 0.01	0.09 ± 0.01
7 - 8	0.83 ± 0.01	0.16 ± 0.01	0.87 ± 0.01	0.12 ± 0.01
8 - 9	0.82 ± 0.01	0.15 ± 0.01	0.84 ± 0.01	0.13 ± 0.01
9 - 12	0.86 ± 0.01	0.15 ± 0.01	0.87 ± 0.01	0.14 ± 0.01

Table 6.8: The results of gaussian fits to the E_T^{L2}/E_T^{LES} distributions for electron volunteers. The rows represent intervals in E_T^{LES} .

GeV E_T^{L2} threshold,

$$s(E_T^{ana}) = \frac{\left(\frac{5.0\text{GeV}}{E_T^{ana}}\right) - \mu(E_T^{ana})}{\sigma(E_T^{ana})},$$

then the efficiency as a function of E_T^{ana} is given by

$$\epsilon(E_T^{ana}) = \begin{cases} 1 - \text{Erf}(s), & s \geq 0 \\ \text{Erf}(s), & s < 0 \end{cases}$$

where $\text{Erf}(x)$ is the error function.

The efficiency of the E_T^{L2} threshold was estimated with the method outlined above. The estimate was then compared to the actual efficiency, which was determined by explicitly applying the $E_T^{L2} > 5$ GeV requirement. The estimate of the efficiency assumed that μ and σ were flat in E_T^{ana} . Further, the magnitudes of μ and σ were taken to be the average values in the interval $8 < E_T^{ana} < 12$ GeV, after the imposition of the E_T^{L2} threshold. The comparison between the estimated and actual values is shown in figure 6.35. The error bars associated with estimated points were obtained by varying the values of μ and σ within one standard deviation. The comparison between the actual efficiency and the estimate is reasonable, the average magnitude of the deviation over the turn-on region being 4.6%.

E_T Range (GeV)	$e\mu$ OS-SS	
	Fitted μ	Fitted σ
5 - 6	0.94 ± 0.01	0.07 ± 0.01
6 - 7	0.88 ± 0.01	0.07 ± 0.01
7 - 8	0.92 ± 0.01	0.08 ± 0.01
8 - 9	0.93 ± 0.02	0.11 ± 0.01
9 - 12	0.91 ± 0.03	0.14 ± 0.02

Table 6.9: The results of gaussian fits to the sign-subtracted E_T^{L2}/E_T^{ELES} distributions for electrons passing the $e\mu$ trigger. The rows represent intervals in E_T^{ELES} .

The same estimation method was applied to the $e\mu$ data. Figure 6.36 shows the distribution of E_T^{L2}/E_T^{na} in the $e\mu$ data, for five intervals in E_T^{na} . Also shown are the gaussian likelihood fits to the distributions. The fitted means and standard deviations are listed in table 6.9. Again, μ and σ were assumed flat in E_T^{na} and taken to be equal to their average values in the interval $8 < E_T^{na} < 12$: $\mu = 0.91 \pm 0.02$, $\sigma = 0.13 \pm .02$. The resulting efficiency for $E_T^{L2} > 5$ GeV is shown in figure 6.37. The error bars represent variations of μ and σ within one standard deviation. From consideration of the above study, a systematic uncertainty of 10% was assigned.

The efficiency of the Level 2 HAD/EM requirement was determined from Monte Carlo. $b\bar{b}$ events were generated and then passed through a CDF detector simulation and a CDF trigger simulation. The simulated events were then reconstructed with the same routines used to reconstruct the data. The resulting efficiency of the $HAD/EM < 0.125$ requirement is shown in figure 6.38 as a function of the reconstructed electron E_T . The efficiency is seen to decrease with increasing E_T ; the higher E_T electrons tending to come from b quarks with a greater Lorentz boost and hence, less isolation from the b hadronic remnants. To build confidence in the result, the scalar sum of the E_T in a cone about the electron was compared

between the data and the simulation. Figures 6.39 and 6.40 show the comparison between the sign-subtracted sum E_T distributions from the data with the simulation, for cones of radius 0.4 and 0.7 in $\eta - \phi$ respectively. The distributions from the simulation include the effects of the trigger simulation and all cuts placed upon the $e\mu$ data.

The efficiency of the final Level 2 requirement, a matching CFT track with $P_T > 4.8$ GeV/c, was determined in a separate analysis [13]. The efficiency of this requirement is shown in figure 6.41 as a function of the reconstructed track P_T . The efficiency was estimated from a sample of reconstructed tracks, taken from events unbiased by triggers utilizing the CFT. A reconstructed track was considered to have passed if it was matched spatially with a CFT track with $P_T > 4.8$ GeV/c.

6.6.2 The Total Trigger Efficiency

$P_T(\mu) > (\text{GeV}/c)$	ϵ_{trig}
3.0	$0.56 \pm 0.02 \pm 0.01$
4.0	$0.61 \pm 0.02 \pm 0.01$
5.0	$0.65 \pm 0.03 \pm 0.01$

Table 6.10: Total trigger efficiency for three values of the offline muon P_T threshold. The first uncertainty reflects the uncertainties of the individual trigger requirements added in quadrature. The second uncertainty corresponds to uncertainties in the shape of the lepton E_T and P_T distributions. The total efficiency was obtained by convoluting the efficiencies of the individual trigger requirements with the normalized lepton P_T and E_T spectra.

The total trigger correction, ϵ_{trig} , was obtained by weighting the individual efficiencies by the P_T and E_T distributions observed in the data. The data were binned in three dimensions: $P_T(\mu)$, $P_T(e)$, and $E_T(e)$. For each bin, a total trigger correction was obtained by taking the product of the efficiencies of the individual trigger requirements. The total correction for that bin was then weighted by the fraction of the total data contained in that bin. The total

trigger correction for the entire data was obtained by summing the weighted corrections for each bin. Table 6.10 shows ϵ_{trig} and the associated uncertainties for three values of the muon P_T threshold. The first uncertainty listed in the table corresponds to the uncertainties of the individual trigger requirements added in quadrature. The second uncertainty corresponds to the uncertainty in the shapes of the observed P_T and E_T spectra. Variations in the shapes of the spectra were studied by parameterizing the observed distributions and then using the parameterizations to generate trial spectra with the same number of events. The trial spectra were convoluted with the efficiencies of the trigger requirements, as detailed above, to obtain a total efficiency, ϵ_{trig}^{gen} . The distribution of ϵ_{trig}^{gen} for several hundred trials was fit with a gaussian. The standard deviation of the fitted gaussian was taken to be the uncertainty associated with variations in the shapes of the P_T and E_T spectra.

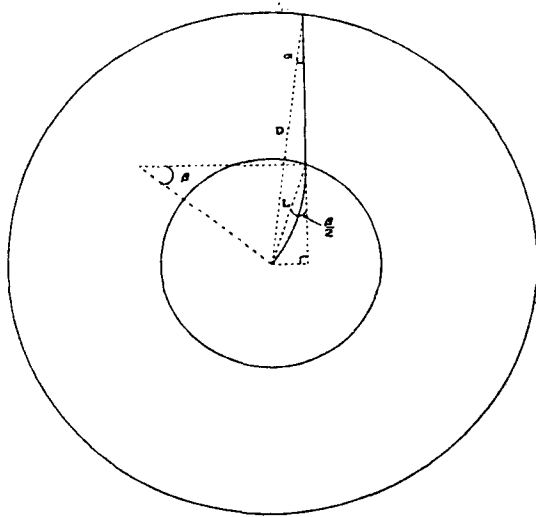


Figure 6.31: Geometry relating muon P_T to angle of incidence at CMU.

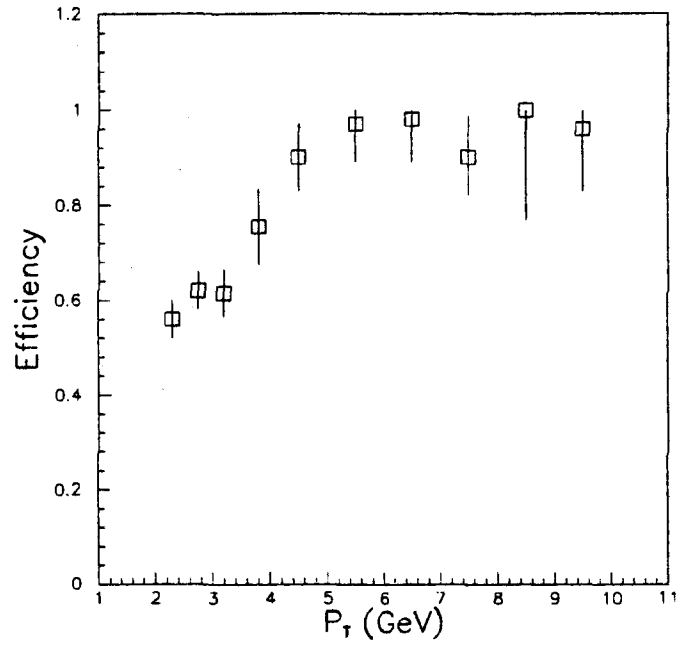


Figure 6.32: The efficiency of the Level 1 muon trigger as a function of the CTC track P_T (from reference [11]).

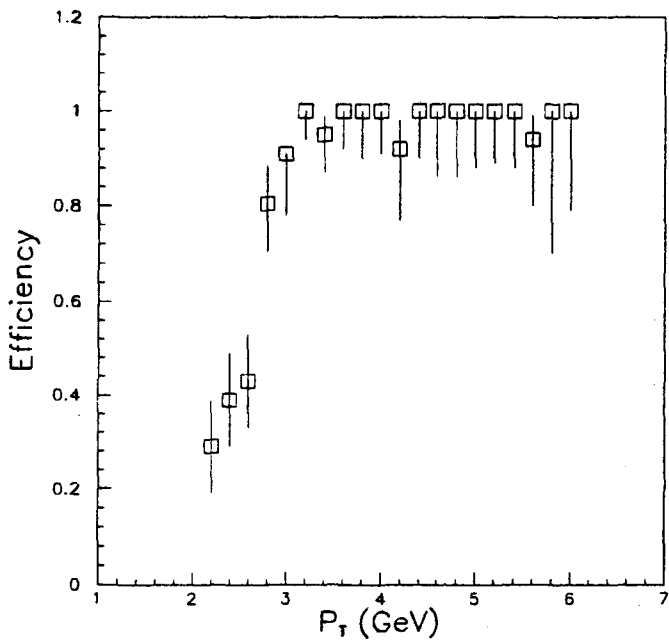


Figure 6.33: The efficiency of the Level 2 muon trigger as a function of the CTC track P_T (from reference [11]).

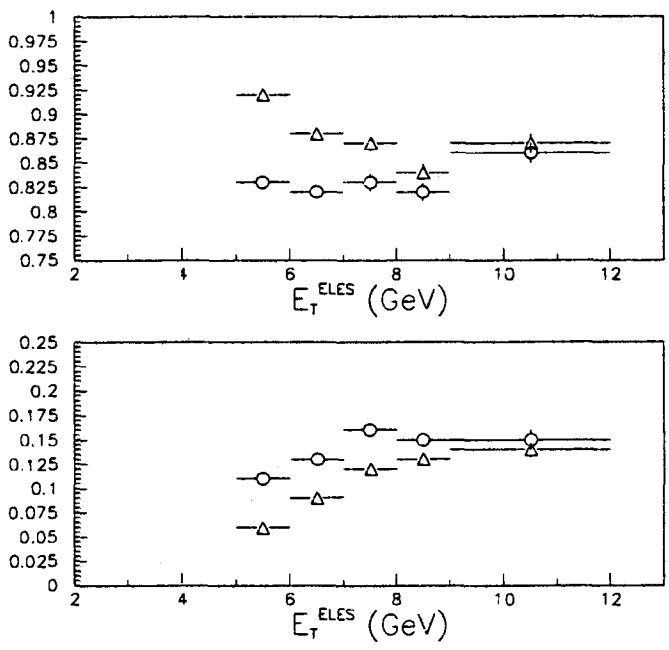


Figure 6.34: Upper: the fitted mean value of the $\frac{E_T^{L^2}}{E_T^{AN^2}}$ distribution for volunteer electrons as a function of the reconstructed electron E_T . Lower: the fitted standard deviation of the $\frac{E_T^{L^2}}{E_T^{AN^2}}$ distribution for volunteer electrons as a function of reconstructed electron E_T . In both cases, circles represent all electrons and triangles those electrons with $E_T^{L^2} > 5$ GeV.

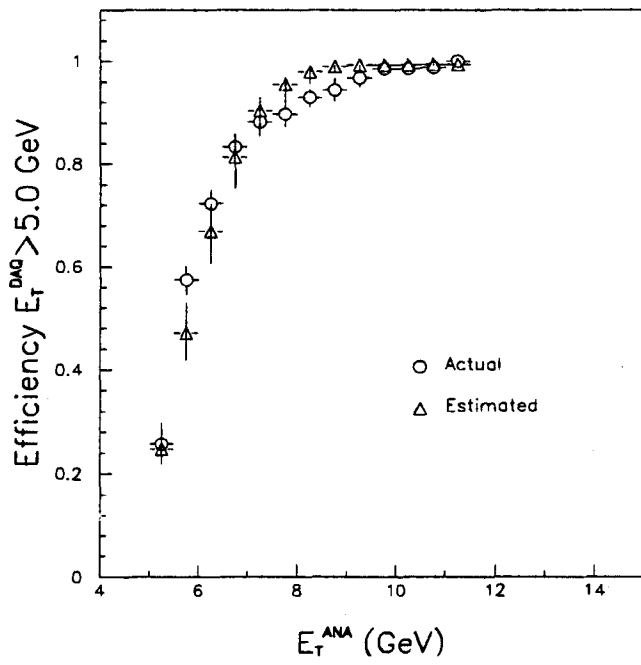


Figure 6.35: A comparison of the estimated efficiency of the 5 GeV L2 E_T threshold for volunteer electrons with the actual efficiency.

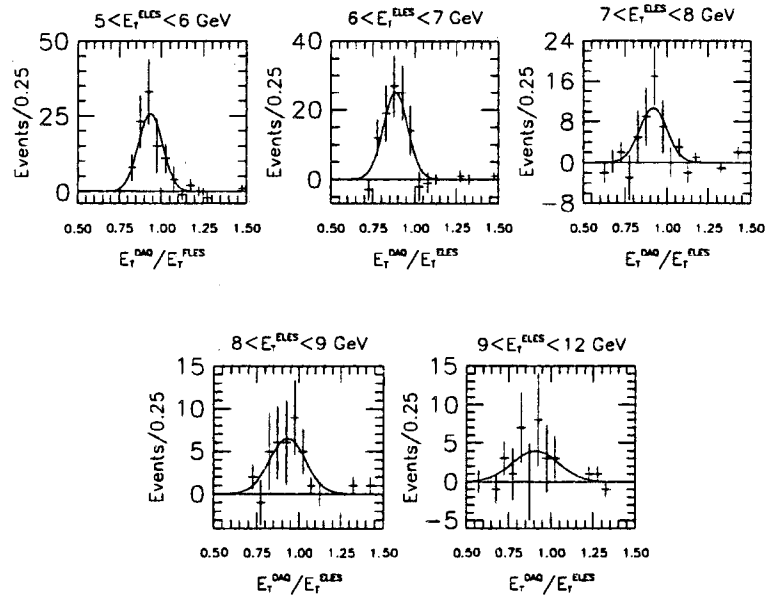


Figure 6.36: The $\frac{E_T^{DAQ}}{E_T^{ANA}}$ distributions for electrons from the $e\mu$ data. Starting from the upper right and proceeding clockwise, the E_T^{ANA} intervals represented are: $5 < E_T^{ANA} < 6$ GeV, $6 < E_T^{ANA} < 7$ GeV, $7 < E_T^{ANA} < 8$ GeV, $8 < E_T^{ANA} < 9$ GeV, and $9 < E_T^{ANA} < 12$ GeV.

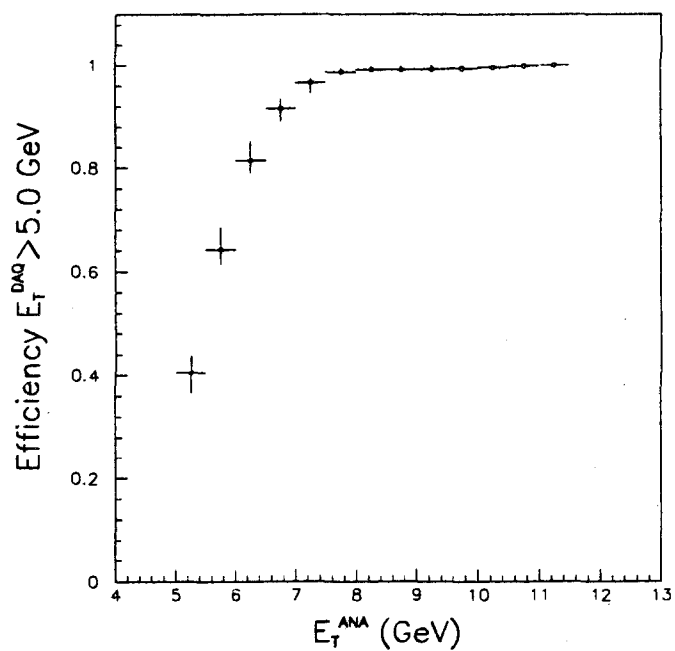


Figure 6.37: The estimated efficiency of the 5 GeV L2 E_T threshold as a function of the reconstructed electron E_T .

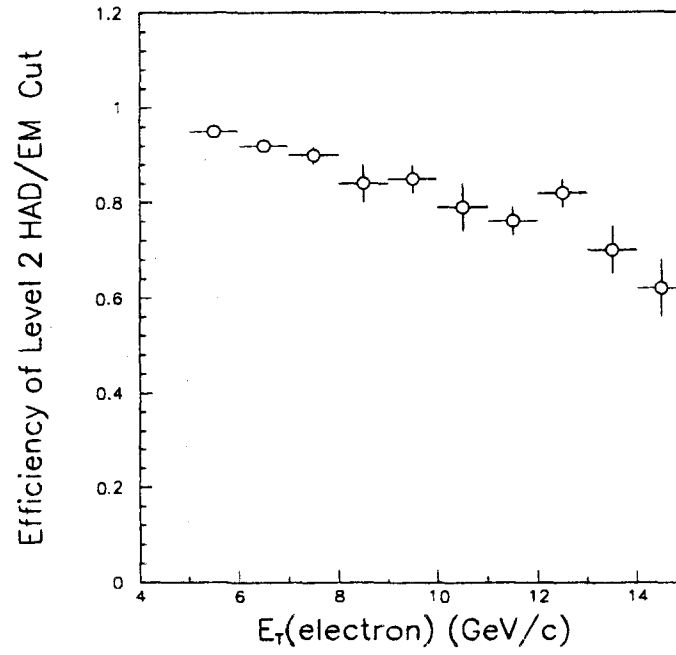


Figure 6.38: The efficiency of the Level 2 *HAD/EM* requirement as determined from ISAJET plus TRGSIM.

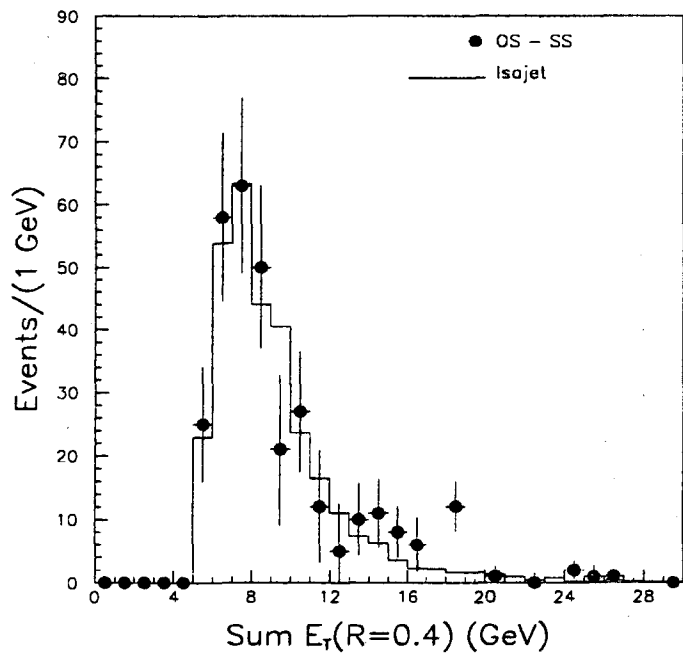


Figure 6.39: The sign-subtracted sum E_T in a cone of 0.4 around the electron. The points represent the $e\mu$ data. The histogram is the prediction from the simulation. The simulation is normalized to the data.

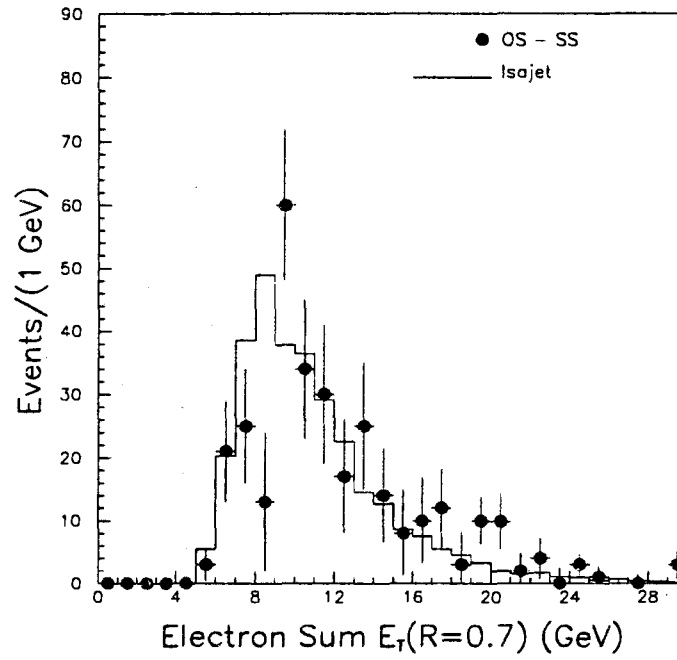


Figure 6.40: The sign-subtracted sum E_T in a cone of 0.7 around the electron. The points represent the $e\mu$ data. The histogram is the prediction from the simulation. The simulation is normalized to the data.

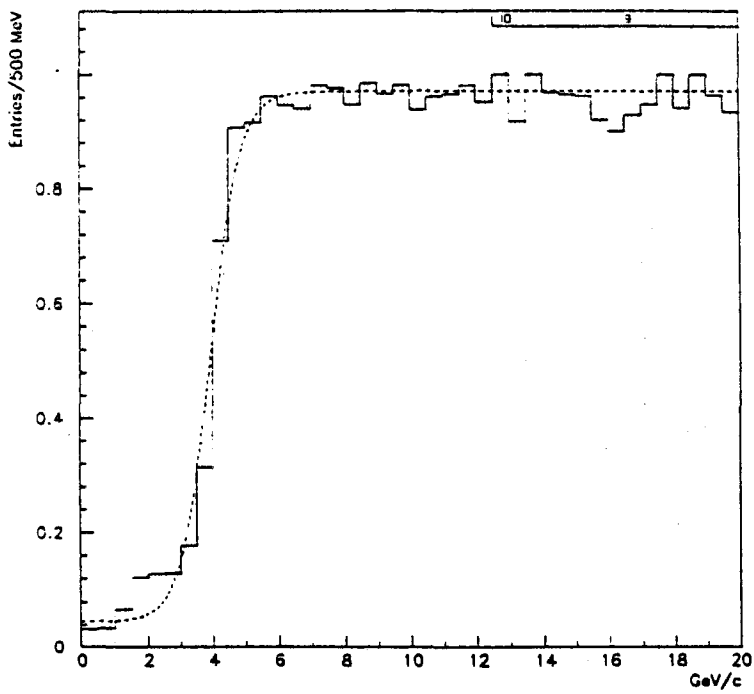


Figure 6.41: The electron tracking efficiency as a function of the CTC track P_T (from reference [12]).

6.7 Results

6.7.1 The Inclusive $b\bar{b}$ Cross Section

$P_T(\mu) > (\text{GeV}/c)$	3.0	4.0	5.0
$P_T^{min} (\text{GeV}/c)$	6.50	7.50	8.75
A (%)	1.77 ± 0.45	1.51 ± 0.39	1.41 ± 0.36
$f_{surv}^{(1)}$	0.35 ± 0.09	0.37 ± 0.09	0.37 ± 0.09
ϵ_{cuts}	0.69 ± 0.27	0.52 ± 0.21	0.41 ± 0.20
ϵ_{trig}	0.56 ± 0.10	0.61 ± 0.10	0.65 ± 0.10
$\Delta_{e\mu}$	248 ± 33	190 ± 25	115 ± 18
\mathcal{L}	$2.65 \pm 0.17 \text{ pb}^{-1}$		
χ	0.16 ± 0.04		
$Br(b \rightarrow eX)$	0.107 ± 0.005		
$Br(b \rightarrow \mu X)$	0.103 ± 0.005		

Table 6.11: Quantities used in the calculation of the cross section for $p\bar{p} \rightarrow b\bar{b} X$.

Table 6.11 summarizes the quantities used to calculate the cross section for $p\bar{p} \rightarrow b\bar{b} X$ with $|y_b| < 1$, $|y_{\bar{b}}| < 1$, and $M_{e\mu} > 5 \text{ GeV}/c^2$. Figure 6.42 compares the cross section to the theoretical expectation from MNR. The cross section is plotted versus the P_T^{min} of the muon-producing b , given the P_T^{min} of the electron-producing b . The inner error bars represent the statistical uncertainty; the outer represent the combined statistical plus systematic uncertainty. The uncertainties are highly correlated between points, tending to change the overall normalization of the cross section more than the shape. The shape of the cross section is seen to compare well to the theoretical expectation over the small range of P_T^{min2} spanned by the data. Although the normalization of the cross section is higher than the central value of the theoretical expectation by approximately a factor of two, this represents only one standard deviation due to the large systematic uncertainties in the measurement. This factor of two is noted to be consistent with previous measurements of the cross section

for $p\bar{p} \rightarrow bX$ at CDF [2]. The dashed lines in the figure represent the uncertainty associated with the theoretical prediction. The theoretical uncertainty was estimated by varying the free parameters of the calculation: the b mass, m_b ; the renormalization scale, Λ_{QCD}^4 ; and the factorization scale, μ . The mass of the b was taken to be $4.75 \text{ GeV}/c^2$ and was varied in the range $4.50 < m_b < 5.00 \text{ GeV}/c^2$. The renormalization scale was taken to be 260 MeV and was varied in the range $160 < \Lambda_{QCD}^4 < 360 \text{ MeV}$. The factorization scale was defined as $\mu = \sqrt{m_b^2 + P_T^2}$ and was varied from $\frac{1}{2}\mu$ to 2μ .

6.7.2 The Single Inclusive b Cross Section

As a check, the MNR calculation was used to find the equivalent single-inclusive b cross section for the measured double-inclusive cross section. The calculation was used to find the ratio

$$\frac{\sigma_{thc}(bX)}{\sigma_{thc}(b\bar{b}X)} = \frac{\sigma(p\bar{p} \rightarrow bX : P_T^b > P_{T,1}^{min}, |y_b| < 1)}{\sigma(p\bar{p} \rightarrow b_1 b_2 X : P_{T,1} > P_{T,1}^{min}, |y_1| < 1; P_{T,2} > P_{T,2}^{min}, |y_2| < 1; M_{e\mu} > 5)}$$

The equivalent single-inclusive cross section was then defined as

$$\sigma(bX) \equiv \frac{\sigma_{thc}(bX)}{\sigma_{thc}(b\bar{b}X)} \sigma(b\bar{b}X).$$

Figure 6.43 shows the comparison between the equivalent single-inclusive b cross section and previous CDF results.

6.7.3 The $e\mu$ Transverse Opening Angle

The opening angle between the b and \bar{b} in the transverse plane, $\Delta\phi_{b\bar{b}}$ was not fully reconstructable using exclusive decay modes. The transverse opening angle between the electron and muon, $\Delta\phi_{e\mu}$, was instead studied as an estimator of $\Delta\phi_{b\bar{b}}$. The sign-subtracted $\Delta\phi_{e\mu}$ distribution for the data is compared with the theoretical prediction (MNR) in figure 6.44. The theoretical prediction is shown normalized to the data, and is in good agreement with the shape of the data distribution. The theoretical prediction for $M_{e\mu} > 0$ is also shown, to demonstrate the effect of the invariant mass cut upon the opening angle; this distribution is normalized to the data with $\Delta\phi_{e\mu} > 100^\circ$.

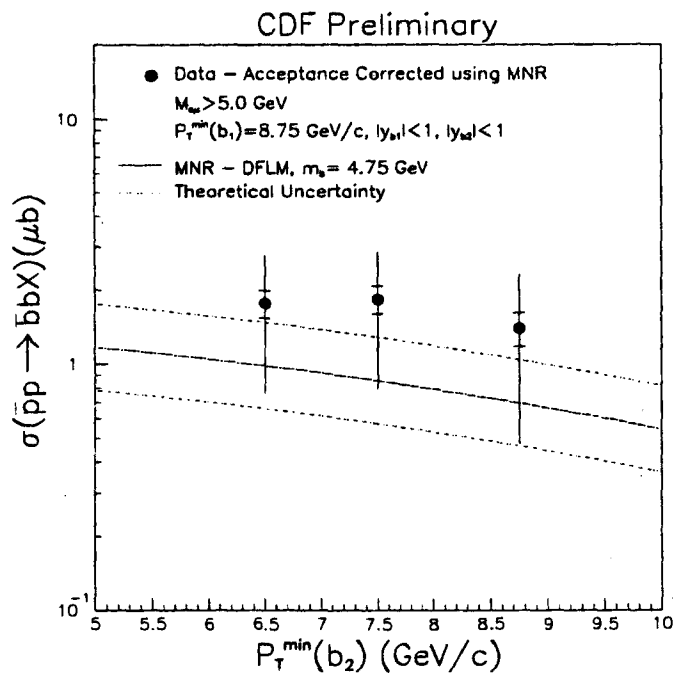


Figure 6.42: The cross section for $p\bar{p} \rightarrow b\bar{b}X$ compared to the theoretical expectation from NLO QCD. The cross section is plotted as a function of the P_T^{\min} of the second b , given the P_T^{\min} of the first. The inner error bars represent the statistical uncertainty; the outer represent the combined statistical plus systematic uncertainty. The dashed lines show the uncertainty associated with the theoretical calculation.

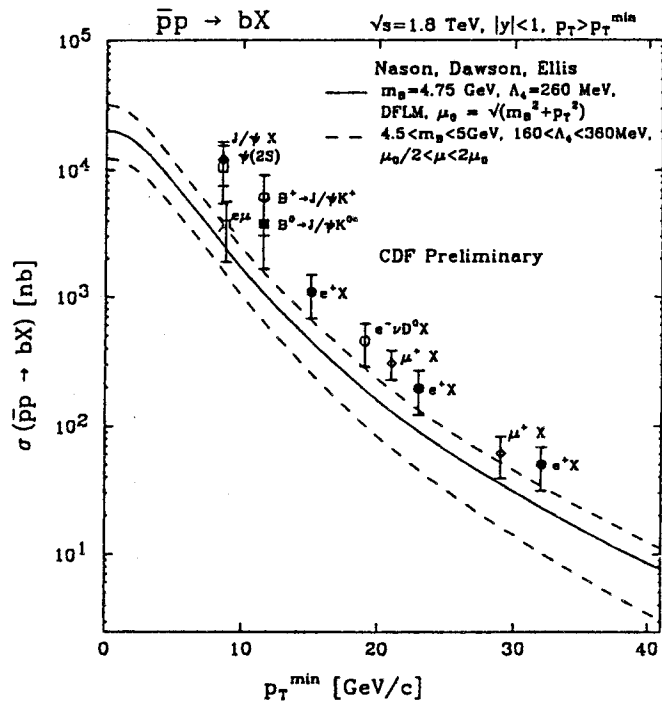


Figure 6.43: The equivalent single-inclusive b cross section from the $e\mu$ data compared to previous CDF measurements and the prediction from NLO QCD.

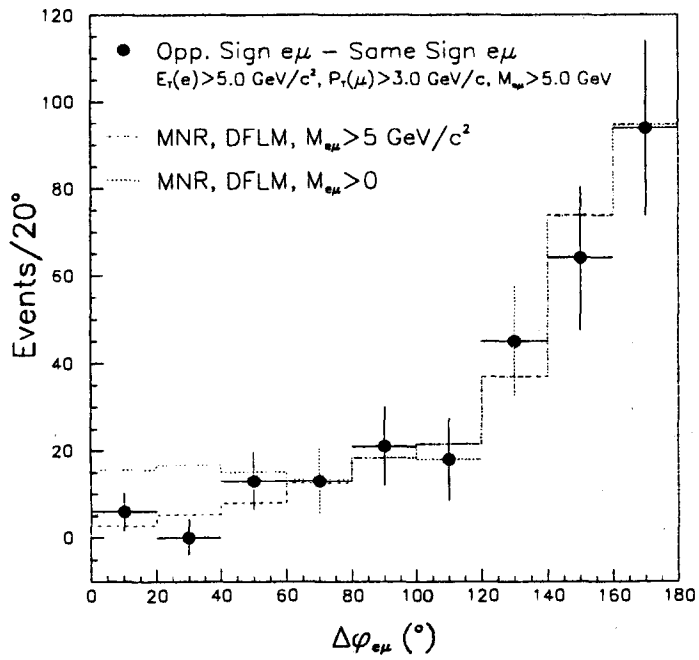


Figure 6.44: The opening angle between the electron and muon in the transverse plane. The data points are sign-subtracted. The lines are the theoretical expectation for $M_{e\mu} > 5 \text{ GeV}/c^2$ and $M_{e\mu} > 0 \text{ GeV}/c^2$.

Chapter 7

Conclusion and Future Prospects

7.0.4 Conclusion

This thesis has presented a measurement of the cross section for the inclusive production of $b\bar{b}$ pairs in $p\bar{p}$ collisions. Comparison of this result to the full $\mathcal{O}(\alpha_s^3)$ calculation of Quantum Chromodynamics shows the theoretical prediction to be low by a factor of two. Due to the large systematic uncertainty associated with the measurement, however, this discrepancy constitutes a difference of only one standard deviation. Notice must also be paid to the large theoretical uncertainty associated with the μ dependence of the QCD calculation. Aside from the absolute normalization, the shape of the predicted cross section compares well to the data, indicating that the theory correctly handles P_T correlations between the quarks. Further, the good agreement between the equivalent single inclusive b cross section and previous CDF measurements is also a good indication that the theory accurately models the $b\bar{b}$ correlations. The good agreement between the observed distribution of $e\mu$ transverse opening angles and the theory implies that spatial correlations are also well described.

Considering the large systematic uncertainties, the discrepancy between the measured cross section for inclusive $b\bar{b}$ production and the $\mathcal{O}(\alpha_s^3)$ QCD prediction should, by itself, not be considered a definitive proof of the inadequacy of the calculation. However, when considered alongside previous CDF measurements of inclusive and exclusive single b cross sections at low P_T , the $b\bar{b}$ result provides further indications that the current theoretical understanding of bottom quark production remains incomplete.

7.0.5 The Future of $b\bar{b}$ Physics at CDF

The future prospects for the investigation of $b\bar{b}$ production at CDF are bright. Aside from higher integrated luminosity, detector upgrades promise increased ability to study b production. Improvements in muon coverage, electron and muon background rejection and improved muon triggering will all aid in the next measurement. The most important upgrade, however, is the installation of a silicon vertex detector that will allow the direct observation of B decays through the reconstruction of displaced vertices. More data, better lepton identification, increased muon acceptance, and the ability to detect displaced vertices will all contribute to a much improved measurement of the inclusive $b\bar{b}$ cross section.

Bibliography

- [1] C. Albajar, *et. al.*, Phys. Lett. **B256** (1991).
- [2] F. Abe, *et. al.*, Phys. Rev. Lett. **68**, 3403-3407 (1992); F. Abe, *et. al.*, Phys. Rev. Lett. **69**, 3704-3708 (1992); F. Abe, *et. al.*, Phys. Rev. Lett. **71**, 501-504 (1993)
- [3] J. D. Bjorken, Phys. Rev. **163**, 1767 (1967)
- [4] R. P. Feynman, *Photon-Hadron Interactions*, Benjamin (1972)
- [5] M. Gell-Mann, Phys. Rev. **125**, 1067 (1962)
- [6] M. Diemoz, *et. al.*, Z. Phys. **C39**, 21 (1988)
- [7] J. T. Friedman, H. W. Kendall, Ann. Rev. Nucl. Science, **22**, 203 (1972)
- [8] F. Abe, *et. al.*, Nucl. Instrum. Methods Phys. Res., Sect. A **271**, 387 (1988)
- [9] R. M. Harris, CDF Note 1329 (1991)
- [10] H. A. Bethe, Phys. Reports **89**, 1256 (1953)
- [11] D. Frei, CDF Note 1430 (1991)
- [12] R. E. Hughes, Ph.D. Thesis, University of Pennsylvania, 1992

- [13] S. Vejcik, Ph.D. Thesis, The Johns Hopkins University, 1992
- [14] P. Nason, S. Dawson, and R.K. Ellis, Nucl. Phys. **B327** ,49 (1989).
- [15] N. Isgur, D. Scora, B. Grinstein, and M.B. Wise, Phys. Rev. **D39** (1989).
- [16] Particle Data Group, *Review of Particle Properties*, Phys. Lett. **B239** (1990).
- [17] D. Bortoletto, *et. al.*, Phys. Rev. **D37**, 1719 (1988)
- [18] C. Peterson, *et. al.*, Phys. Rev. **D27**, 105 (1983)
- [19] M. Mangano, P. Nason, and G. Ridolfi, Nucl. Phys. **B373** ,295-345 (1992).

F. Abe,¹² M. Albrow,⁶ D. Amidei,¹⁵ C. Anway-Wiese,³ G. Apollinari,²³ M. Atac,⁶
 P. Auchincloss,²² P. Azzi,¹⁷ N. Bacchetta,¹⁶ A. R. Baden,⁸ W. Badgett,¹⁵ M. W. Bailey,²¹
 A. Bamberger,^{6,a} P. de Barbaro,²² A. Barbaro-Galtieri,¹³ V. E. Barnes,²¹ B. A. Barnett,¹¹
 P. Bartalini,²⁰ G. Bauer,¹⁴ T. Baumann,⁸ F. Bedeschi,²⁰ S. Behrends,² S. Belforte,²⁰
 G. Bellettini,²⁰ J. Bellinger,²⁸ D. Benjamin,²⁷ J. Benlloch,¹⁴ J. Bensinger,² A. Beretvas,⁶
 J. P. Berge,⁶ S. Bertolucci,⁷ K. Biery,¹⁰ S. Bhadra,⁹ M. Binkley,⁶ D. Bisello,¹⁷ R. Blair,¹
 C. Blocker,² A. Bodek,²² V. Bolognesi,²⁰ A. W. Booth,⁶ C. Boswell,¹¹ G. Brandenburg,⁸
 D. Brown,⁸ E. Buckley-Geer,⁶ H. S. Budd,²² G. Busetto,¹⁷ A. Byon-Wagner,⁶ K. L. Byrum,¹
 C. Campagnari,⁸ M. Campbell,¹⁵ A. Caner,⁶ R. Carey,⁸ W. Carithers,¹³ D. Carlsmith,²⁸
 J. T. Carroll,⁶ R. Cashmore,^{6,a} A. Castro,¹⁷ Y. Cen,¹⁸ F. Cervelli,²⁰ K. Chadwick,⁶
 J. Chapman,¹⁵ G. Chiarelli,⁷ W. Chinowsky,¹³ S. Cihangir,⁶ A. G. Clark,⁶ M. Cobal,²⁰
 D. Connor,¹⁸ M. Contreras,⁴ J. Cooper,⁶ M. Cordelli,⁷ D. Crane,⁶ J. D. Cunningham,²
 C. Day,⁶ F. DeJongh,⁶ S. Dell'Agnello,²⁰ M. Dell'Orso,²⁰ L. Demortier,²³ B. Denby,⁶
 P. F. Derwent,¹⁵ T. Devlin,²⁴ M. Dickson,²² S. Donati,²⁰ R. B. Drucker,¹³ A. Dunn,¹⁵
 K. Einsweiler,¹³ J. E. Elias,⁶ R. Ely,¹³ S. Eno,⁴ S. Errede,⁹ A. Etchegoyen,^{6,a} B. Farhat,¹⁴
 M. Frantschi,¹⁶ G. J. Feldman,⁸ B. Flaugher,⁶ G. W. Foster,⁶ M. Franklin,⁸ J. Freeman,⁶
 H. Frisch,⁴ T. Fuess,⁶ Y. Fukui,¹² G. Gagliardi,²⁰ A. F. Garfinkel,²¹ A. Gauthier,⁹
 S. Geer,⁶ D. W. Gerdes,¹⁵ P. Giannetti,²⁰ N. Giokaris,²³ P. Giromini,⁷ L. Gladney,¹⁸
 M. Gold,¹⁶ J. Gonzalez,¹⁸ K. Goulianos,²³ H. Grassmann,¹⁷ G. M. Grieco,²⁰ R. Grindley,¹⁰
 C. Grosso-Pilcher,⁴ C. Haber,¹³ S. R. Hahn,⁶ R. Handler,²⁸ K. Hara,²⁶ B. Harral,¹⁸
 R. M. Harris,⁶ S. A. Hauger,⁵ J. Hauser,³ C. Hawk,²⁴ T. Hessing,²⁵ R. Hollebeek,¹⁸
 L. Holloway,⁹ A. Hölscher,¹⁰ S. Hong,¹⁵ G. Houk,¹⁸ P. Hu,¹⁹ B. Hubbard,¹³ B. T. Huffman,¹⁹
 R. Hughes,²² P. Hurst,⁸ J. Huth,⁶ J. Huyen,⁶ M. Incagli,²⁰ T. Ino,²⁶ H. Iso,²⁶ H. Jensen,⁶
 C. P. Jessop,⁸ R. P. Johnson,⁶ U. Joshi,⁶ R. W. Kadel,¹³ T. Kamon,²⁵ S. Kanda,²⁶
 D. A. Kardelis,⁹ I. Karliner,⁹ E. Kearns,⁸ L. Keeble,²⁵ R. Kephart,⁶ P. Kestun,²
 R. M. Keup,⁹ H. Keutelian,⁶ D. Kim,⁶ S. B. Kim,¹⁵ S. H. Kim,²⁶ Y. K. Kim,¹³
 L. Kirsch,² K. Kondo,²⁶ J. Konigsberg,⁸ K. Kordas,¹⁰ E. Kovacs,⁶ M. Krasberg,¹⁵
 S. E. Kuhlmann,¹ E. Kuns,²⁴ A. T. Laasanen,²¹ S. Lammel,³ J. I. Lamoureux,²⁸ S. Leone,²⁰
 J. D. Lewis,⁶ W. Li,¹ P. Limon,⁶ M. Lindgren,³ T. M. Liss,⁹ N. Lockyer,¹⁸ M. Loreti,¹⁷
 E. H. Low,¹⁸ D. Lucchesi,²⁰ C. B. Luchini,⁹ P. Lukens,⁶ P. Maas,²⁸ K. Maeshima,⁶
 M. Mangano,²⁰ J. P. Marriner,⁶ M. Mariotti,²⁰ R. Markeloff,²⁸ L. A. Markosky,²⁸
 J. A. J. Matthews,¹⁶ R. Mattingly,² P. McIntyre,²⁵ A. Menzione,²⁰ E. Meschi,²⁰ T. Meyer,²⁵
 S. Mikamo,¹² M. Miller,⁴ T. Mimashi,²⁶ S. Miscetti,⁷ M. Mishina,¹² S. Miyashita,²⁶
 Y. Morita,²⁶ S. Moulding,²³ J. Mueller,²⁴ A. Mukherjee,⁶ T. Muller,³ L. F. Nakae,²
 I. Nakano,²⁶ C. Nelson,⁶ D. Neuberger,³ C. Newman-Holmes,⁶ J. S. T. Ng,⁸ M. Ninomiya,²⁶
 L. Nodulman,¹ S. Ogawa,²⁶ C. Pagliarone,²⁰ R. Paoletti,²⁰ V. Papadimitriou,⁶ A. Para,⁶
 E. Pare,⁸ S. Park,⁶ J. Patrick,⁶ G. Pauletta,²⁰ L. Pescara,¹⁷ T. J. Phillips,⁵ A. G.
 Piacentino,²⁰ R. Plunkett,⁶ L. Pondrom,²⁸ J. Proudfoot,¹ F. Ptohos,⁸ G. Punzi,²⁰
 D. Quarrie,⁶ K. Ragan,¹⁰ G. Redlinger,⁴ J. Rhoades,²⁸ M. Roach,²⁷ F. Rimondi,^{6,a}
 L. Ristori,²⁰ W. J. Robertson,⁵ T. Rodrigo,⁶ T. Rohaly,¹⁸ A. Roodman,⁴ W. K. Sakumoto,²²
 A. Sansoni,⁷ R. D. Sard,⁹ A. Savoy-Navarro,⁶ V. Scarpine,⁹ P. Schlabach,⁸ E. E. Schmidt,⁶

O. Schneider,¹³ M. H. Schub,²¹ R. Schwitters,⁹ G. Sciacca,²⁰ A. Scribano,²⁰ S. Segler,⁶ S. Seidel,¹⁶ Y. Seiya,²⁶ G. Sganos,¹⁰ M. Shapiro,¹³ N. M. Shaw,²¹ M. Sheaff,²⁸ M. Shochet,⁴ J. Siegrist,¹³ A. Sill,²² P. Sinervo,¹⁰ J. Skarha,¹¹ K. Sliwa,²⁷ D. A. Smith,²⁰ F. D. Snider,¹¹ L. Song,⁶ T. Song,¹⁵ M. Spahn,¹³ P. Sphicas,¹⁴ A. Spies,¹¹ R. St. Denis,⁸ L. Stanco,¹⁷ A. Stefanini,²⁰ G. Sullivan,⁴ K. Sumorok,¹⁴ R. L. Swartz, Jr.,⁹ M. Takano,²⁶ K. Takikawa,²⁶ S. Tarem,² F. Tartarelli,²⁰ S. Tether,¹⁴ D. Theriot,⁶ M. Timko,²⁷ P. Tipton,²² S. Tkaczyk,⁶ A. Tollestrup,⁶ J. Tonnison,²¹ W. Trischuk,⁸ Y. Tsay,⁴ J. Tseng,¹¹ N. Turini,²⁰ F. Ukegawa,²⁶ D. Underwood,¹ S. Vejcek, III,¹⁵ R. Vidal,⁶ R. G. Wagner,¹ R. L. Wagner,⁶ N. Wainer,⁵ R. C. Walker,²² J. Walsh,¹⁸ A. Warburton,¹⁰ G. Watts,²² T. Watts,²⁴ R. Webb,²⁵ C. Wendt,²⁸ H. Wenzel,²⁰ W. C. Wester, III,¹³ T. Westhusing,⁹ S. N. White,²³ A. B. Wicklund,¹ E. Wicklund,⁶ H. H. Williams,¹⁸ B. L. Winer,²² J. Wolinski,²⁵ D. Y. Wu,¹⁵ X. Wu,²⁰ J. Wyss,¹⁷ A. Yagil,⁶ W. Yao,¹³ K. Yasuoka,²⁶ Y. Ye,¹⁰ G. P. Yeh,⁶ J. Yoh,⁶ M. Yokoyama,²⁶ J. C. Yun,⁶ A. Zanetti,²⁰ F. Zetti,²⁰ S. Zhang,¹⁵ W. Zhang,¹⁸ S. Zucchelli,^{6,a}

The CDF Collaboration

¹ Argonne National Laboratory, Argonne, Illinois 60439

² Brandeis University, Waltham, Massachusetts 02254

³ University of California at Los Angeles, Los Angeles, California 90024

⁴ University of Chicago, Chicago, Illinois 60637

⁵ Duke University, Durham, North Carolina 27706

⁶ Fermi National Accelerator Laboratory, Batavia, Illinois 60510

⁷ Laboratori Nazionali di Frascati, Istituto Nazionale di Fisica Nucleare, Frascati, Italy

⁸ Harvard University, Cambridge, Massachusetts 02138

⁹ University of Illinois, Urbana, Illinois 61801

¹⁰ Institute of Particle Physics, McGill University, Montreal, and University of Toronto, Toronto, Canada

¹¹ The Johns Hopkins University, Baltimore, Maryland 21218

¹² National Laboratory for High Energy Physics (KEK), Japan

¹³ Lawrence Berkeley Laboratory, Berkeley, California 94720

¹⁴ Massachusetts Institute of Technology, Cambridge, Massachusetts 02139

- 15 *University of Michigan, Ann Arbor, Michigan 48109*
- 16 *University of New Mexico, Albuquerque, New Mexico 87131*
- 17 *Università di Padova, Istituto Nazionale di Fisica Nucleare, Sezione di Padova, I-35131 Padova, Italy*
- 18 *University of Pennsylvania, Philadelphia, Pennsylvania 19104*
- 19 *University of Pittsburgh, Pittsburgh, Pennsylvania 15260*
- 20 *Istituto Nazionale di Fisica Nucleare, University and Scuola Normale Superiore of Pisa, I-56100 Pisa, Italy*
- 21 *Purdue University, West Lafayette, Indiana 47907*
- 22 *University of Rochester, Rochester, New York 14627*
- 23 *Rockefeller University, New York, New York 10021*
- 24 *Rutgers University, Piscataway, New Jersey 08854*
- 25 *Texas A&M University, College Station, Texas 77843*
- 26 *University of Tsukuba, Tsukuba, Ibaraki 305, Japan*
- 27 *Tufts University, Medford, Massachusetts 02155*
- 28 *University of Wisconsin, Madison, Wisconsin 53706*